



# Calculation of predictions for non-identical particle correlations in heavy ions collisions at LHC energies from hydrodynamics-inspired models

MASTER OF SCIENCE THESIS

Author:  
**Mateusz Wojciech Gałażyn**

Supervisor:  
**Prof. Adam Kisiel**

Warsaw, 12th November 2014



# Wyznaczenie przewidywań teoretycznych dla korelacji cząstek nieidentycznych w zderzeniach ciężkich jonów przy energiach LHC w modelach opartych na hydrodynamice

PRACA MAGISTERSKA

Autor:  
**Mateusz Wojciech Gałażyn**

Promotor:  
**dr hab. inż. Adam Kisiel, prof. PW**

Warszawa, 12 listopada 2014

**Abstract**

## **Streszczenie**

# <sup>3</sup> Contents

<sup>4</sup>	<b>Introduction</b>	<b>1</b>
<sup>5</sup>	<b>1 Theory of heavy ion collisions</b>	<b>2</b>
<sup>6</sup>	1.1 The Standard Model . . . . .	2
<sup>7</sup>	1.2 Quantum Chromodynamics . . . . .	3
<sup>8</sup>	1.2.1 Quarks and gluons . . . . .	3
<sup>9</sup>	1.2.2 Quantum Chromodynamics potential . . . . .	4
<sup>10</sup>	1.2.3 The quark-gluon plasma . . . . .	6
<sup>11</sup>	1.3 Relativistic heavy ion collisions . . . . .	7
<sup>12</sup>	1.3.1 Stages of heavy ion collision . . . . .	7
<sup>13</sup>	1.3.2 QGP signatures . . . . .	9
<sup>14</sup>	<b>2 Therminator model</b>	<b>17</b>
<sup>15</sup>	2.1 (3+1)-dimensional viscous hydrodynamics . . . . .	17
<sup>16</sup>	2.2 Statistical hadronization . . . . .	18
<sup>17</sup>	2.2.1 Cooper-Frye formalism . . . . .	19
<sup>18</sup>	<b>3 Particle interferometry</b>	<b>21</b>
<sup>19</sup>	3.1 HBT interferometry . . . . .	21
<sup>20</sup>	3.2 Theoretical approach . . . . .	22
<sup>21</sup>	3.2.1 Conventions used . . . . .	22
<sup>22</sup>	3.2.2 Two particle wave function . . . . .	23
<sup>23</sup>	3.2.3 Source emission function . . . . .	24
<sup>24</sup>	3.2.4 Theoretical correlation function . . . . .	26
<sup>25</sup>	3.2.5 Spherical harmonics decomposition of a correlation function	27
<sup>26</sup>	3.3 Experimental approach . . . . .	28
<sup>27</sup>	3.4 Scaling of femtoscopic radii . . . . .	29
<sup>28</sup>	3.4.1 Scaling in LCMS . . . . .	30
<sup>29</sup>	3.4.2 Scaling in PRF . . . . .	30
<sup>30</sup>	<b>4 Results</b>	<b>32</b>
<sup>31</sup>	4.1 Identical particles correlations . . . . .	32
<sup>32</sup>	4.1.1 Spherical harmonics components . . . . .	32
<sup>33</sup>	4.1.2 Centrality dependence of a correlation function . . . . .	36

34	4.1.3 $k_T$ dependence of a correlation function . . . . .	37
35	4.2 Results of the fitting procedure . . . . .	38
36	4.2.1 The three-dimensional femtoscopic radii scaling . . . . .	38
37	4.2.2 Scaling of one-dimensional radii . . . . .	42
38	4.3 Discussion of the results . . . . .	43
39	<b>Conclusions</b>	<b>44</b>

<sup>40</sup> **Introduction**

<sup>41</sup> **Chapter 1**

<sup>42</sup> **Theory of heavy ion collisions**

<sup>43</sup> **1.1 The Standard Model**

<sup>44</sup> In the 1970s, a new theory of fundamental particles and their interaction  
<sup>45</sup> emerged. A new concept, which concerns the electromagnetic, weak and strong  
<sup>46</sup> nuclear interactions between known particles. This theory is called *The Standard*  
<sup>47</sup> *Model*. There are seventeen named particles in the standard model, organized  
<sup>48</sup> into the chart shown below (Fig. 1.1). Fundamental particles are divided into  
two families: *fermions* and *bosons*.

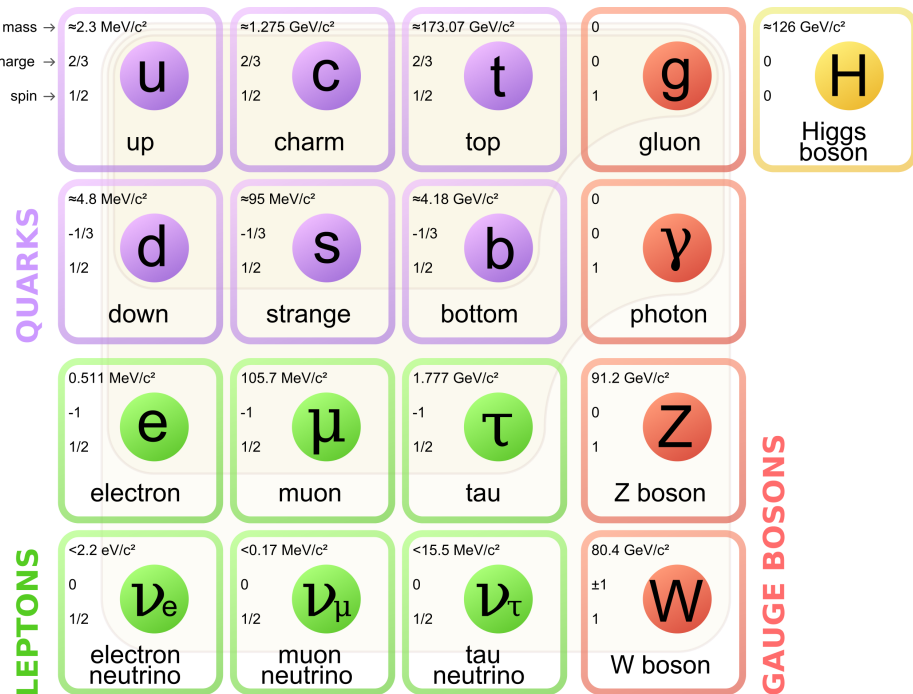


Figure 1.1: The Standard Model of elementary particles [1].

49 Fermions are the building blocks of matter. They are divided into two groups.  
 50 Six of them, which must bind together are called *quarks*. Quarks are known to  
 51 bind into doublets (*mesons*), triplets (*baryons*) and recently confirmed four-quark  
 52 states.<sup>1</sup> Two of baryons, with the longest lifetimes, are forming a nucleus: a pro-  
 53 ton and a neutron. A proton is build from two up quarks and one down, and  
 54 neutron consists of two down quarks and one up. A proton is found to be a stable  
 55 particle (at least it has a lifetime larger than  $10^{35}$  years) and a free neutron has a  
 56 mean lifetime about  $8.8 \times 10^2$  s. Fermions, that can exist independently are called  
 57 *leptons*. Neutrinos are a subgroup of leptons, which are only influenced by weak  
 58 interaction. Fermions can be divided into three generations (three columns in  
 59 the Figure 1.1). Generation I particles can combine into hadrons with the longest  
 60 life spans. Generation II and III consists of unstable particles which form also  
 61 unstable hadrons.

62 Bosons are force carriers. There are four fundamental forces: weak - respons-  
 63ible for radioactive decay, strong - coupling quarks into hadrons, electromagnetic  
 64 - between charged particles and gravity - the weakest, which causes the attraction  
 65 between particles with a mass. The Standard Model describes the first three. The  
 66 weak force is mediated by  $W^\pm$  and  $Z^0$  bosons, electromagnetic force is carried by  
 67 photons  $\gamma$  and the carriers of a strong interaction are gluons  $g$ . The fifth boson is  
 68 a Higgs boson which is responsible for giving other particles mass.

## 69 1.2 Quantum Chromodynamics

### 70 1.2.1 Quarks and gluons

71 Quarks interact with each other through the strong interaction. The mediator  
 72 of this force is a *gluon* - a massless and chargeless particle. In the quantum chro-  
 73 modynamics (QCD) - theory describing strong interaction - there are six types of  
 74 "charges" (like electrical charges in the electrodynamics) called *colours*. The col-  
 75 ours were introduced because some of the observed particles, like  $\Delta^-$ ,  $\Delta^{++}$  and  
 76  $\Omega^-$  appeared to consist of three quarks with the same flavour ( $ddd$ ,  $uuu$  and  $sss$   
 77 respectively), which was in conflict with the Pauli principle. One quark can carry  
 78 one of the three colours (usually called *red*, *green* and *blue*) and antiquark one of  
 79 the three anti-colours respectively. Only colour-neutral (or white) particles could  
 80 exist. Mesons are assumed to be a colour-anticolour pair, while baryons are *red-*  
 81 *green-blue* triplets. Gluons also are colour-charged and there are 8 types of gluons.  
 82 Therefore they can interact with themselves [3].

---

<sup>1</sup>The LHCb experiment at CERN in Geneva confirmed recently existence of  $Z(4430)$  - a particle consisting of four quarks [2].

83    **1.2.2 Quantum Chromodynamics potential**

84       As a result of that gluons are massless, one can expect, that the static potential  
 85       in the QCD will have the similar form like one in the electrodynamics e.g.  $\sim 1/r$   
 86       (through an analogy to photons). In reality the QCD potential is assumed to have  
 87       the form of [3]

$$V_s = -\frac{4}{3} \frac{\alpha_s}{r} + kr, \quad (1.1)$$

88       where the  $\alpha_s$  is a coupling constant of the strong force and the  $kr$  part is related  
 89       with the *confinement*. In comparison to the electromagnetic force, a value of the  
 90       strong coupling constant is  $\alpha_s \approx 1$  and the electromagnetic one is  $\alpha = 1/137$ .

91       The fact that quarks does not exist separately, but they are always bound,  
 92       is called a confinement. As two quarks are pulled apart, the linear part  $kr$  in  
 93       the Eq. 1.1 becomes dominant and the potential becomes proportional to the dis-  
 94       tance. This situation resembles stretching of a string. At some point, when the  
 95       string is so large it is energetically favourable to create a quark-antiquark pair. At  
 96       this moment such pair (or pairs) is formed, the string breaks and the confinement  
 97       is preserved (Fig. 1.2).

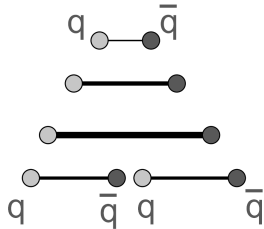


Figure 1.2: A string break and a creation of a pair quark-anti-quark [4].

97       On the other hand, for the small  $r$ , an interaction between the quarks and  
 98       gluons is dominated by the Coulomb-like term  $-\frac{4}{3} \frac{\alpha_s}{r}$ . The coupling constant  $\alpha_s$   
 99       depends on the four-momentum  $Q^2$  transferred in the interaction. This depend-  
 100      ence is presented in Fig. 1.3. The value  $\alpha_s$  decreases with increasing momentum  
 101      transfer and the interaction becomes weak for large  $Q^2$ , i.e.  $\alpha_s(Q) \rightarrow 0$ . Be-  
 102      cause of weakening of coupling constant, quarks at large energies (or small dis-  
 103      tances) are starting to behave like free particles. This phenomenon is known as  
 104      an *asymptotic freedom*. The QCD potential has also temperature dependence - the  
 105      force strength "melts" with the temperature increase. Therefore the asymptotic  
 106      freedom is expected to appear in either the case of high baryon densities (small  
 107      distances between quarks) or very high temperatures. This temperature depend-  
 108      ence is illustrated in the Fig. 1.4.

109       If the coupling constant  $\alpha_s$  is small, one can use perturbative methods to cal-  
 110      culate physical observables. Perturbative QCD (pQCD) successfully describes  
 111      hard processes (with large  $Q^2$ ), such as jet production in high energy proton-  
 112      antiproton collisions. The applicability of pQCD is defined by the *scale parameter*

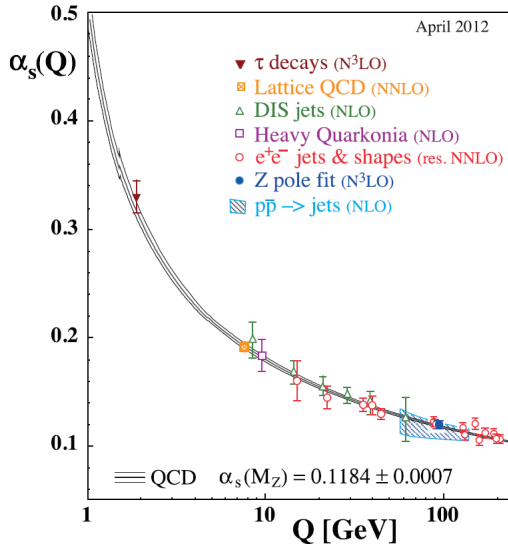


Figure 1.3: The coupling parameter  $\alpha_s$  dependence on four-momentum transfer  $Q^2$  [5].

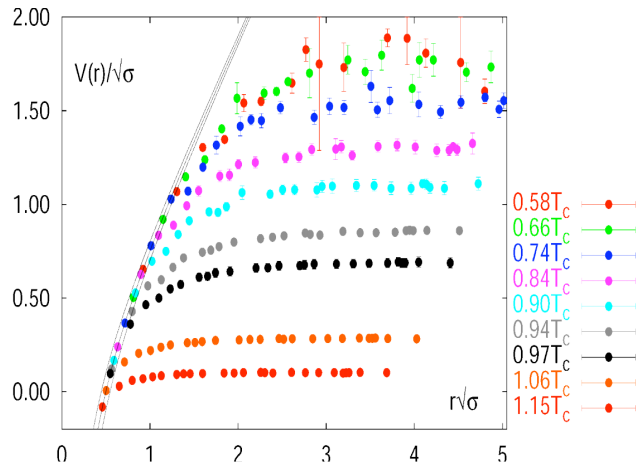


Figure 1.4: The QCD potential for a pair quark-antiquark as a function of distance for different temperatures. A value of a potential decreases with the temperature [4].

<sup>114</sup>  $\Lambda_{QCD} \approx 200$  MeV. If  $Q \gg \Lambda_{QCD}$  then the process is in the perturbative domain  
<sup>115</sup> and can be described by pQCD. A description of soft processes (when  $Q < 1$  GeV)  
<sup>116</sup> is a problem in QCD - perturbative theory breaks down at this scale. Therefore,  
<sup>117</sup> to describe processes with low  $Q^2$ , one has to use alternative methods like Lattice  
<sup>118</sup> QCD. Lattice QCD (LQCD) is non-perturbative implementation of a field theory  
<sup>119</sup> in which QCD quantities are calculated on a discrete space-time grid. LQCD al-

lows to obtain properties of matter in equilibrium, but there are some limitations.  
Lattice QCD requires fine lattice spacing to obtain precise results - therefore large  
computational resources are necessary. With the constant growth of computing  
power this problem will become less important. The second problem is that lat-  
tice simulations are possible only for baryon density  $\mu_B = 0$ . At  $\mu_B \neq 0$ , Lattice  
QCD breaks down because of the sign problem [6].

### 1.2.3 The quark-gluon plasma

The new state of matter in which quarks are no longer confined is known as a *quark-gluon plasma* (QGP). The predictions coming from the discrete space-time Lattice QCD calculations reveal a phase transition from the hadronic matter to the quark-gluon plasma at the high temperatures and baryon densities. The res-

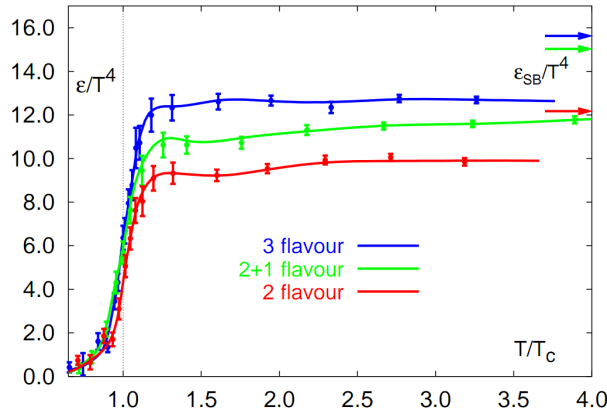


Figure 1.5: A number of degrees of freedom as a function of a temperature [7].

ults obtained from such calculations are shown on Fig. 1.5. The energy density  $\epsilon$  which is divided by  $T^4$  is a measure of number of degrees of freedom in the system. One can observe significant rise of this value, when the temperature increases past the critical value  $T_C$ . Such increase is signaling a phase transition - the formation of QGP [8]. The values of the energy densities plotted in Fig. 1.5 do not reach the Stefan-Boltzmann limit  $\epsilon_{SB}$  (marked with arrows), which corresponds to an ideal gas. This can indicate some residual interactions in the system. According to the results from the RHIC<sup>2</sup>, the new phase of matter behaves more like an ideal fluid, than like a gas [9].

One of the key questions, to which current heavy ion physics tries to find an answer is the value of a critical temperature  $T_C$  as a function of a baryon chemical potential  $\mu_B$  (baryon density), where the phase transition occur. The results coming from the Lattice QCD are presented in the Fig. 1.6. The phase of matter in which quarks and gluons are deconfined is expected to exist at large

<sup>2</sup>Relativistic Heavy Ion Collider at Brookhaven National Laboratory in Upton, New York

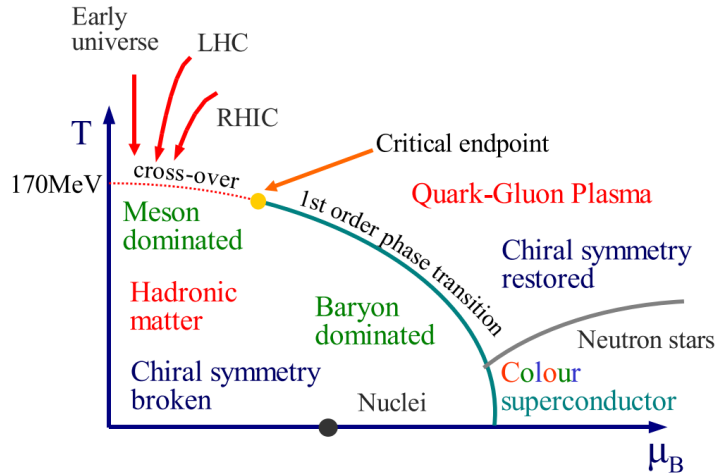


Figure 1.6: Phase diagram coming from the Lattice QCD calculations [8].

temperatures. In the region of small temperatures and high baryon densities, a different state is supposed to appear - a *colour superconductor*. The phase transition between hadronic matter and QGP is thought to be of 1<sup>st</sup> order at  $\mu_B \gg 0$ . However as  $\mu_B \rightarrow 0$  quarks' masses become significant and a sharp transition transforms into a rapid but smooth cross-over. It is believed that in Pb-Pb collisions observed at the LHC<sup>3</sup>, the created matter has high enough temperature to be in the quark-gluon plasma phase, then cools down and converts into hadrons, undergoing a smooth transition [8].

### 1.3 Relativistic heavy ion collisions

#### 1.3.1 Stages of heavy ion collision

To create the quark-gluon plasma one has to achieve high enough temperatures and baryon densities. Such conditions can be recreated in the heavy ion collisions at the high energies. The left side of the Figure 1.7 shows simplified picture of a central collision of two highly relativistic nuclei in the centre-of-mass reference frame. The colliding nuclei are presented as thin disks because of the Lorentz contraction. In the central region, where the energy density is the highest, a new state of matter - the quark-gluon plasma - is supposedly created. Afterwards, the plasma expands ad cools down, quarks combine into hadrons and their mutual interactions cease when the system reaches the *freeze-out* temperature. Subsequently, produced free hadrons move towards the detectors.

On the right side of the Figure 1.7 there is presented a space-time evolution of a collision process, plotted in the light-cone variables ( $z, t$ ). The two highly

<sup>3</sup>Large Hadron Collider at CERN, Geneva

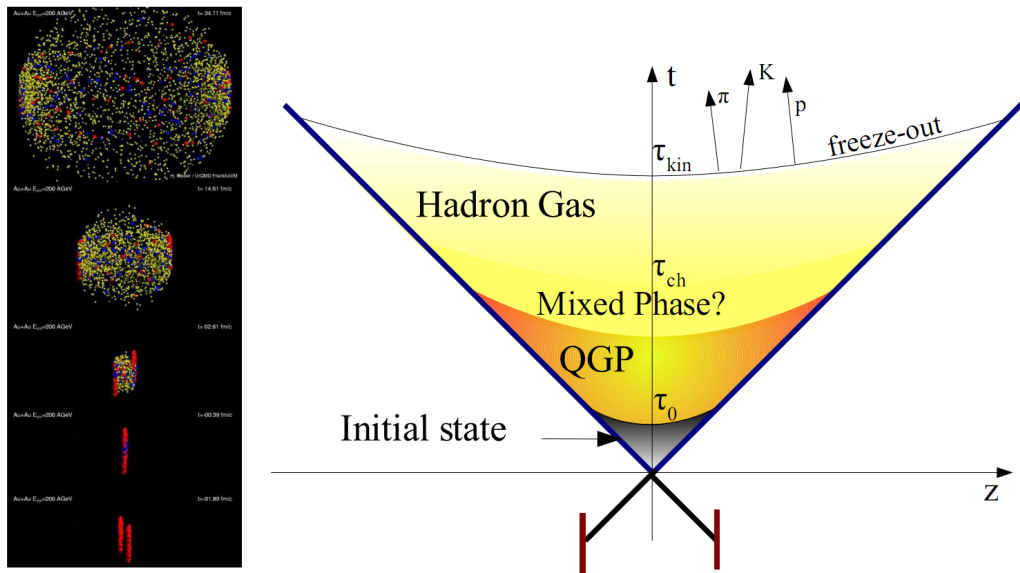


Figure 1.7: Left: stages of a heavy ion collision simulated in the UrQMD model. Right: schematic view of a heavy ion collision evolution [8].

167 relativistic nuclei are traveling basically along the light cone until they collide  
 168 at the centre of diagram. Nuclear fragments emerge from the collision again  
 169 along the (forward) light cone, while the matter between fragmentation zones  
 170 populates the central region. This hot and dense matter is believed to be in the  
 171 state of the quark-gluon plasma. There exist several frameworks to describe this  
 172 transition to the QGP phase, for example: QCD string breaking, QCD parton cas-  
 173 cades or colour glass condensate evolving into glasma and later into quark-gluon  
 174 plasma [10].

175 **String breaking** – In the string picture, the nuclei pass through each other forming  
 176 colour strings. This is analogous to the situation depicted in the Fig 1.2 - the  
 177 colour string is created between quarks inside particular nucleons in nuclei. In  
 178 the next step strings decay / fragment forming quarks and gluons or directly  
 179 hadrons. This approach becomes invalid at very high energies, when the strings  
 180 overlap and cannot be treated as independent objects.

181 **Parton cascade** – The parton<sup>4</sup> cascade model is based on the pQCD. The col-  
 182 liding nuclei are treated as clouds of quarks and which penetrate through each  
 183 other. The key element of this method is the time evolution of the parton phase-  
 184 space distributions, which is governed by a relativistic Boltzmann equation with  
 185 a collision term that contains dominant perturbative QCD interations. The bot-  
 186 tleneck of the parton cascade model is the low energies regime, where the  $Q^2$  is  
 187 too small to be described by the perturbative theory.

<sup>4</sup>A parton is a common name for a quark and a gluon.

188 **Colour glass condensate** – The colour glass condensate assumes, that the had-  
 189 ron can be viewed as a tightly packed system of interacting gluons. The sat-  
 190 uration of gluons increases with energy, hence the total number of gluons may  
 191 increase without the bound. Such a saturated and weakly coupled gluon system  
 192 is called a colour glass condensate. The fast gluons in the condensate are Lorentz  
 193 contracted and redistributed on the two very thin sheets representing two col-  
 194 liding nuclei. The sheets are perpendicular to the beam axis. The fast gluons  
 195 produce mutually orthogonal colour magnetic and electric fields, that only ex-  
 196 ist on the sheets. Immediately after the collision, i.e. just after the passage of  
 197 the two gluonic sheets after each other, the longitudinal electric and magnetic  
 198 fields are produced forming the *glasma*. The glasma fields decay through the  
 199 classical rearrangement of the fields into radiation of gluons. Also decays due to  
 200 the quantum pair creations are possible. In this way, the quark-gluon plasma is  
 201 produced.

202 Interactions within the created quark-gluon plasma bring the system into the  
 203 local statistical equilibrium, hence its further evolution can be described by the  
 204 relativistic hydrodynamics. The hydrodynamic expansion causes that the sys-  
 205 tem becomes more and more dilute. The phase transition from the quark-gluon  
 206 plasma to the hadronic gas occurs. Further expansion causes a transition from the  
 207 strongly interaction hadronic gas to weakly interacting system of hadrons which  
 208 move freely to the detectors. Such decoupling of hadrons is called the *freeze-out*.  
 209 The freeze-out can be divided into two phases: the chemical freeze-out and the  
 210 thermal one. The *chemical freeze-out* occurs when the inelastic collisions between  
 211 constituents of the hadron gas stop. As the system evolves from the chemical  
 212 freeze-out to the thermal freeze-out the dominant processes are elastic collisions  
 213 (such as, for example  $\pi + \pi \rightarrow \rho \rightarrow \pi + \pi$ ) and strong decays of heavier reso-  
 214 nances which populate the yield of stable hadrons. The *thermal freeze-out* is the  
 215 stage of the evolution of matter, when the strongly coupled system transforms  
 216 to a weakly coupled one (consisting of essentially free particles). In other words  
 217 this is the moment, where the hadrons practically stop to interact. Obviously, the  
 218 temperatures corresponding to the two freeze-outs satisfy the condition

$$T_{chem} > T_{therm}, \quad (1.2)$$

219 where  $T_{chem}$  (inferred from the ratios of hadron multiplicities) is the temperature  
 220 of the chemical freeze-out, and  $T_{therm}$  (obtained from the investigation of the  
 221 transverse-momentum spectra) is the temperature of the thermal freeze-out [10].

### 222 1.3.2 QGP signatures

223 The quark-gluon plasma is a very short living and unstable state of matter.  
 224 One cannot investigate the properties of a plasma and confirm its existence dir-  
 225 ectly. Hence, the several experimental effects were proposed as QGP signatures,  
 226 some of them have been already observed in heavy ion experiments [8]. As mat-  
 227 ter created in the heavy ions collisions is supposed to behave like a fluid, one

should expect appearance of collective behaviour at small transverse momenta - so called *elliptic flow* and *radial flow*. The next signal is the temperature range obtained from the measurements of *direct photons*, which gives us information, that the system created in heavy ion collisions is far above the critical temperature obtained from the LQCD calculations. The *puzzle in the di-lepton spectrum* can be explained by the modification of spectral shape of vector mesons (mostly  $\rho$  meson) in the presence of a dense medium. This presence of a medium can also shed light on the *jet quenching* phenomenon - the suppression occurrence in the high  $p_T$  domain.

### Elliptic flow

In a non-central heavy ion collisions, created region of matter has an almond shape with its shorter axis in the *reaction plane* (Fig. 1.8). The pressure gradient is much larger in-plane rather than out-of-plane. This causes larger acceleration and transverse velocities in-plane rather than out-of-plane. Such differences can

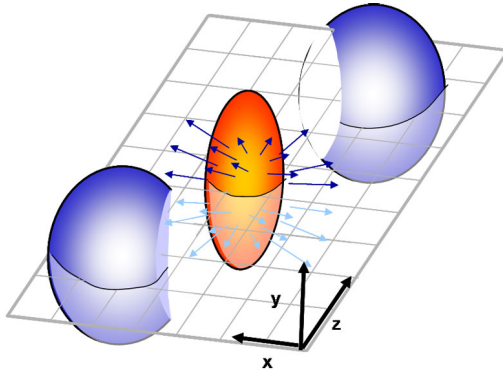


Figure 1.8: Overlapping region which is created in heavy ion collisions has an almond shape. Visible x-z plane is a *reaction plane*. The x-y plane is a *transverse plane*. The z is a direction of the beam [11].

be investigated by studying the distribution of particles with respect to the reaction plane orientation [12]:

$$E \frac{d^3 N}{dp^3} = \frac{1}{2\pi} \frac{d^2 N}{p_T dp_T dy} (1 + 2v_1 \cos(\phi) + 2v_2 \cos(2\phi) + \dots), \quad (1.3)$$

where  $\phi$  is the angle between particle transverse momentum  $p_T$  (a momentum projection on a transverse plane) and the reaction plane,  $N$  is a number of particles and  $E$  is an energy of a particle. The  $y$  variable is a *rapidity* defined as:

$$y = \frac{1}{2} \ln \left( \frac{E + p_L}{E - p_L} \right), \quad (1.4)$$

247 where  $p_L$  is a longitudinal component of a momentum (parallel to the beam direction).  
 248 The  $v_n$  coefficients indicate the shape of a system. For the most central collisions  
 249 ( $b = 0$  - see Fig. 1.9) all coefficients vanish  $\bigwedge_{n \in N_+} v_n = 0$  (the overlapping region has the spherical shape). The Fourier series elements in the parentheses

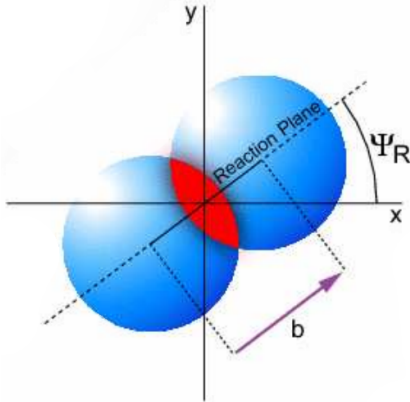


Figure 1.9: Cross-section of a heavy ion collision in a transverse plane.  $\Psi_R$  is an angle between transverse plane and the reaction plane. The  $b$  parameter is an *impact parameter* - a distance between centers of nuclei during a collision. An impact parameter is related with the centrality of a collision and a volume of the quark-gluon plasma [12].

250 in Eq. 1.3 represent different kinds of a flow. The first value: "1" represents the  
 251 *radial flow* - an isotropic flow in every direction. Next coefficient  $v_1$  is responsible  
 252 for *direct flow*. The  $v_2$  coefficient is a measure of elliptic anisotropy (*elliptic flow*).  
 253 The  $v_2$  has to build up in the early stage of a collision - later the system becomes  
 254 too dilute: space asymmetry and the pressure gradient vanish. Therefore the  
 255 observation of elliptic flow means that the created matter was in fact a strongly  
 256 interacting matter.

257 The  $v_2$  coefficient was measured already at CERN SPS, LHC and RHIC. For  
 258 the first time hydrodynamics successfully described the collision dynamics as the  
 259 measured  $v_2$  reached hydrodynamic limit (Fig. 1.10). As expected, there is a mass  
 260 ordering of  $v_2$  as a function of  $p_T$  (lower plot in the Fig. 1.10) with pions having  
 261 the largest and protons the smallest anisotropy. In the upper plots in the Fig. 1.10  
 262 there is a  $v_2$  as a function of transverse kinetic energy. The left plot shows the  
 263 two universal trend lines for baryons and mesons. After the scaling of  $v_2$  and the  
 264 kinetic energy by the number of valence quarks, all of the hadrons follow the  
 265 same universal curve. Those plots show that strong collectivity is observed in  
 266 heavy ion collisions.

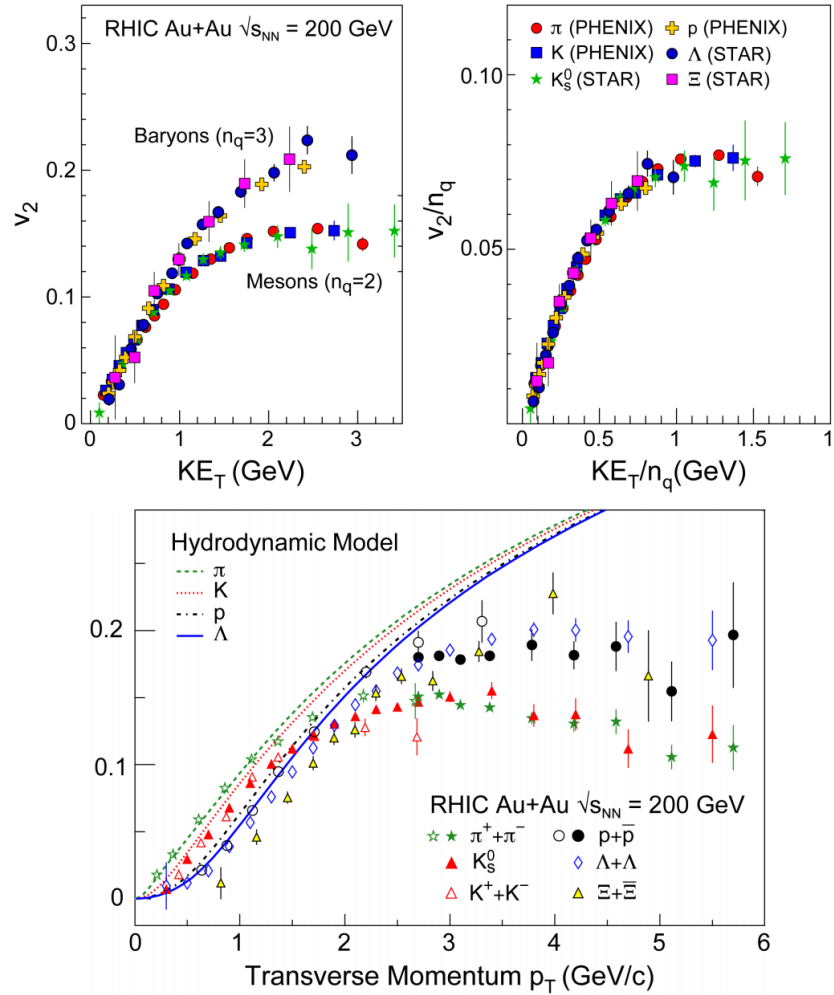


Figure 1.10: *Lower:* The elliptic flow  $v_2$  follows the hydrodynamical predictions for an ideal fluid perfectly. Note that > 99% of all final hadrons have  $p_T < 1.5$  GeV/c. *Upper left:* The  $v_2$  plotted versus transverse kinetic energy  $KE_T = m_T - m_0 = \sqrt{p_T^2 + m_0^2} - m_0$ . The  $v_2$  follows different universal curves for mesons and baryons. *Upper right:* When scaled by the number of valence quarks, the  $v_2$  follows the same universal curve for all hadrons and for all values of scaled transverse kinetic energy [13].

## 268 Transverse radial flow

269 Elliptic flow described previously is caused by the pressure gradients which  
270 must also produce a more simple collective behaviour of matter - a movement  
271 inside-out, called radial flow. Particles are pushed to higher momenta and they  
272 move away from the center of the collision. A source not showing collective

273 behaviour, like pp collisions, produces particle spectra that can be fitted by a  
 274 power-law [8]:

$$\frac{1}{2\pi p_T} \frac{d^2N}{dp_T d\eta} = C \left( 1 + \frac{p_T}{p_0} \right)^{-\gamma}. \quad (1.5)$$

275 The  $\eta$  variable is a *pseudorapidity* defined as follows:

$$\eta = \frac{1}{2} \ln \left( \frac{p + p_L}{p - p_L} \right) = -\ln \left( \frac{\theta}{2} \right), \quad (1.6)$$

where  $\theta$  is an emission angle  $\cos \theta = p_L/p$ .

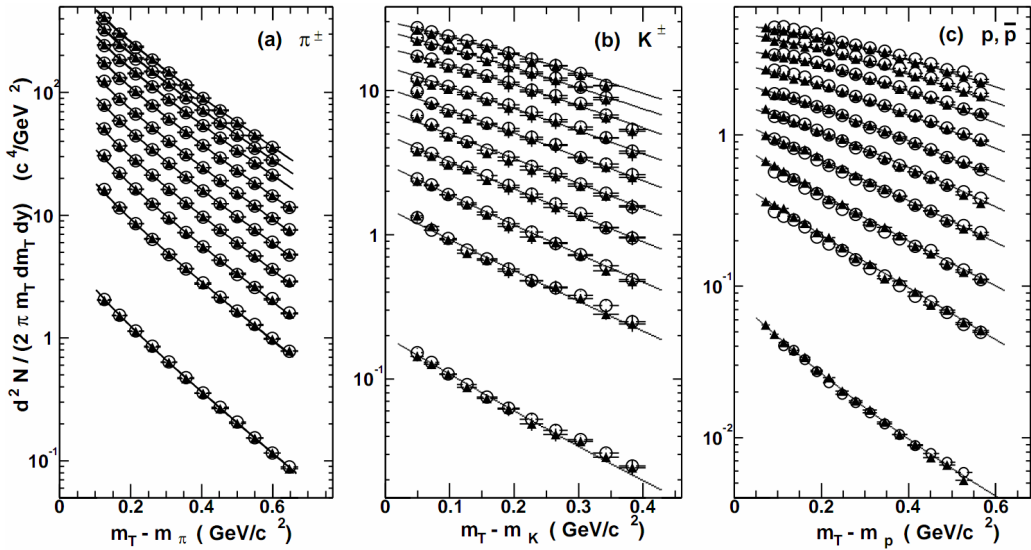


Figure 1.11: Invariant yield of particles versus transverse mass  $m_T = \sqrt{p_T^2 + m_0^2}$  for  $\pi^\pm$ ,  $K^\pm$ ,  $p$  and  $\bar{p}$  at mid-rapidity for p+p collisions (bottom) and Au+Au events from 70-80% (second bottom) to 0-5% (top) centrality [14].

276  
 277 The hydrodynamical expansion of a system gives the same flow velocity kick  
 278 for different kind of particles - ones with bigger masses will gain larger  $p_T$  boost.  
 279 This causes increase of the yield of particles with larger transverse momenta. In  
 280 the invariant yield plots one can observe the decrease of the slope parameter,  
 281 especially for the heavier hadrons. This is presented in the Fig. 1.11. The most  
 282 affected spectra are ones of kaons (b) and protons (c). One can notice decrease  
 283 of the slope parameter for heavy ion collisions (plots from second bottom to top)  
 284 comparing to the proton-proton collisions (bottom ones), where no boost from  
 285 radial flow should occur [8].

### 286 Direct photons

287 The direct photons are photons, which are not coming from the final state  
 288 hadrons decays. Their sources can be various interaction from charged particles

created in the collision, either at the partonic or at the hadronic level. Direct photons are considered to be an excellent probe of the early stage of the collision. This is because their mean free path is very large to the created system in the collision. Thus photons created at the early stage leave the system without suffering any interaction and retain information about this stage, in particular about its temperature.

One can distinguish two kinds of direct photons: *thermal* and *prompt*. Thermal photons can be emitted from the strong processes in the quark-gluon plasma involving quarks and gluons or hot hadronic matter (e.g. processes:  $\pi\pi \rightarrow \rho\gamma$ ,  $\pi\rho \rightarrow \pi\gamma$ ). Thermal photons can be observed in the low  $p_T$  region. Prompt photons are believed to come from “hard” collisions of initial state partons belonging to the colliding nuclei. The prompt photons can be described using the pQCD. They will dominate the high  $p_T$  region. The analysis of transverse momentum of spectra of direct photons revealed, that the temperature of the source of thermal photons produced in heavy ion collisions at RHIC is in the range 300-600 MeV (Fig. 1.12). Hence the direct photons had to come from a system whose temperature is far above from the critical temperature for QGP creation.

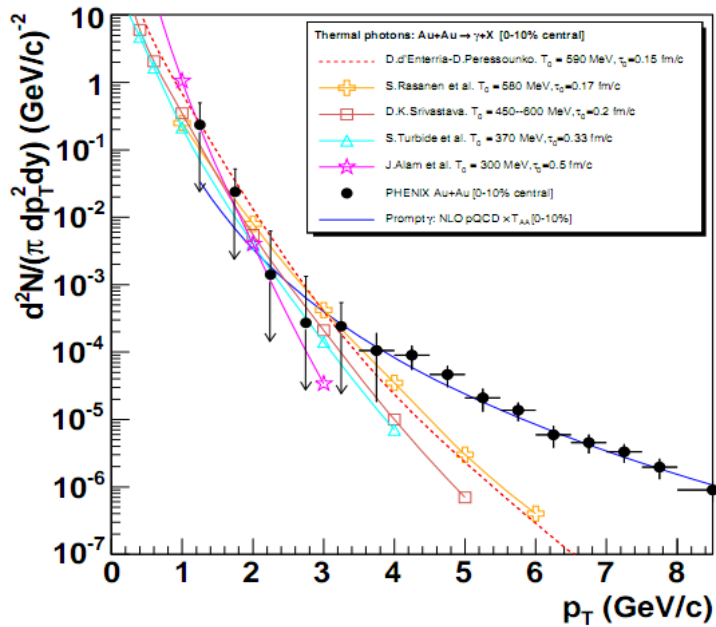


Figure 1.12: Thermal photons spectra for the central Au+Au collisions at  $\sqrt{s_{NN}} = 200$  GeV computed within different hydrodynamical models compared with the pQCD calculations (solid line) and experimental data from PHENIX (black dots) [15].

306 **Puzzle in di-lepton mass spectrum**

307 The invariant mass spectra (Fig. 1.13) of lepton pairs reveal many peaks cor-  
 308 responding to direct decays of various mesons into a lepton pair. The continu-  
 309 ous background in this plot is caused by the decays of hadrons into more than  
 310 two leptons (including so-called *Dalitz decays* into a lepton pair and a photon).  
 Particular hadron decay channels, which contribute to this spectrum are shown

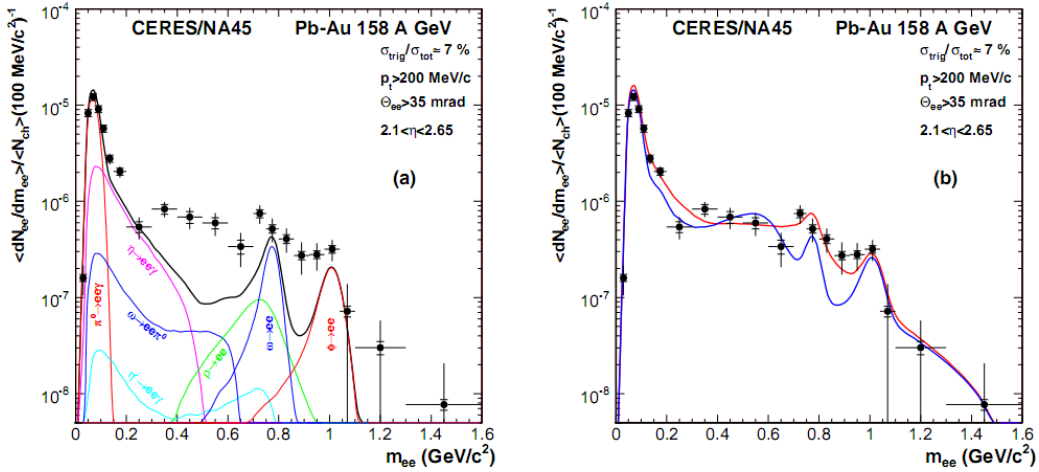


Figure 1.13: Left: Invariant mass spectrum of  $e^+ - e^-$  pairs in  $\text{Pb} + \text{Au}$  collisions at 158A GeV compared to the sum coming from the hadron decays predictions. Right: The expectations coming from model calculations assuming a dropping of the  $\rho$  mass (blue) or a spread of the  $\rho$  width in the medium (red) [16].

311 in the Fig. 1.13 with the coloured lines and their sum with the black one. The  
 312 sum (called *the hadronic cocktail*) of various components describes experimen-  
 313 tal spectra coming from the simple collisions (like  $p + p$  or  $p + A$ ) quite well with the  
 314 statistical and systematical uncertainties [9]. This situation is different consider-  
 315 ing more complicated systems i.e.  $A + A$ . Spectra coming from  $\text{Pb} + \text{Au}$  collisions  
 316 are presented on the plots in the Fig. 1.13. The “hadronic cocktail” does not de-  
 317 scribe the data, in the mass range between the  $\pi$  and the  $\rho$  mesons a significant  
 318 excess of electron pairs over the calculated sum is observed. Theoretical expla-  
 319 nation of this phenomenon assumes modification of the spectral shape of vector  
 320 mesons in a dense medium. Two different interpretations of this increase were  
 321 proposed: a decrease of meson mass with the medium density and increase of the  
 322 meson width in the dense medium. In principle, one could think of simultaneous  
 323 occurrence of both effects: mass shift and resonance broadening. Experimental  
 324 results coming from the CERES disfavour the mass shift hypothesis indicating  
 325 only broadening of resonance peaks (Fig. 1.13b) [9].

327 **Jet quenching**

328 A jet is defined as a group of particles with close vector momenta and high en-  
 329 ergies. It has its beginning when the two partons are going in opposite directions  
 330 and have energy big enough to produce new quark-antiquark pair and then ra-  
 331 diate gluons. This process can be repeated many times and it results in two back-  
 332 to-back jets of hadrons. It has been found that jets in the opposite hemisphere  
 333 (*away-side jets*) show a very different pattern in d+Au and Au+Au collisions. This  
 334 is shown in the azimuthal correlations in the Fig. 1.14. In d+Au collisions, like in  
 335 p+p, a pronounced away-side jet appears around  $\Delta\phi = \pi$ , exactly opposite to the  
 336 trigger jet, what is typical for di-jet events. In central Au+Au collisions the away-  
 jet is suppressed. When the jet has its beginning near the surface of the quark-

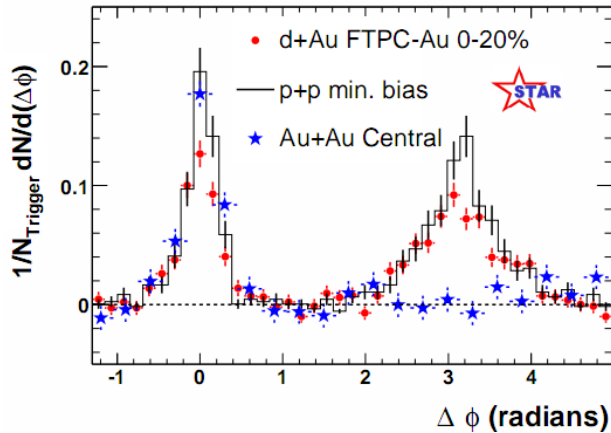


Figure 1.14: Azimuthal angle difference  $\Delta\phi$  distributions for different colliding systems at  $\sqrt{s_{NN}} = 200$  GeV. Transverse momentum cut:  $p_T > 2$  GeV. For the Au+Au collisions the away-side jet is missing [17].

337  
 338 gluon plasma, one of the jets (*near-side jet*) leaves the system almost without any  
 339 interactions. This jet is visible on the correlation plot as a high peak at  $\Delta\phi = 0$ .  
 340 However, the jet moving towards the opposite direction has to penetrate a dense  
 341 medium. The interaction with the plasma causes energy dissipation of particles  
 342 and is visible on an azimuthal correlation plot as disappearance of the away-side  
 343 jet [9].

<sup>344</sup> **Chapter 2**

<sup>345</sup> **Therminator model**

<sup>346</sup> THERMINATOR [18] is a Monte Carlo event generator designed to investigate  
<sup>347</sup> the particle production in the relativistic heavy ion collisions. The functionality  
<sup>348</sup> of the code includes a generation of the stable particles and unstable resonances  
<sup>349</sup> at the chosen hypersurface model. It performs the statistical hadronization which  
<sup>350</sup> is followed by space-time evolution of particles and the decay of resonances. The  
<sup>351</sup> key element of this method is an inclusion of a complete list of hadronic reso-  
<sup>352</sup> nances, which contribute very significantly to the observables. The second version  
<sup>353</sup> of THERMINATOR [19] comes with a possibility to incorporate any shape of freeze-  
<sup>354</sup> out hypersurface and the expansion velocity field, especially those generated ex-  
<sup>355</sup> ternally with various hydrodynamic codes.

<sup>356</sup> **2.1 (3+1)-dimensional viscous hydrodynamics**

<sup>357</sup> Most of the relativistic viscous hydrodynamic calculations are done in  
<sup>358</sup> (2+1)-dimensions. Such simplification assumes boost-invariance of a matter  
<sup>359</sup> created in a collision. Experimental data reveals that no boost-invariant region is  
<sup>360</sup> formed in the collisions [20]. Hence, for the better description of created system  
<sup>361</sup> a (3+1)-dimensional model is required.

<sup>362</sup> In the four dimensional relativistic dynamics one can describe a system  
<sup>363</sup> using a space-time four-vector  $x^\nu = (ct, x, y, z)$ , a velocity four-vector  
<sup>364</sup>  $u^\nu = \gamma(c, v_x, v_y, v_z)$  and a energy-momentum tensor  $T^{\mu\nu}$ . The particular  
<sup>365</sup> components of  $T^{\mu\nu}$  have a following meaning:

- <sup>366</sup> •  $T^{00}$  - an energy density,
- <sup>367</sup> •  $cT^{0\alpha}$  - an energy flux across a surface  $x^\alpha$ ,
- <sup>368</sup> •  $T^{\alpha 0}$  - an  $\alpha$ -momentum flux across a surface  $x^\alpha$  multiplied by  $c$ ,
- <sup>369</sup> •  $T^{\alpha\beta}$  - components of momentum flux density tensor,

370 where  $\gamma = (1 - v^2/c^2)^{-1/2}$  is Lorentz factor and  $\alpha, \beta \in \{1, 2, 3\}$ . Using  $u^\nu$  one can  
 371 express  $T^{\mu\nu}$  as follows [21]:

$$T_0^{\mu\nu} = (e + p)u^\mu u^\nu - pg^{\mu\nu} \quad (2.1)$$

372 where  $e$  is an energy density,  $p$  is a pressure and  $g^{\mu\nu}$  is an inverse metric tensor:

$$g^{\mu\nu} = \begin{bmatrix} 1 & 0 & 0 & 0 \\ 0 & -1 & 0 & 0 \\ 0 & 0 & -1 & 0 \\ 0 & 0 & 0 & -1 \end{bmatrix}. \quad (2.2)$$

373 The presented version of energy-momentum tensor (Eq. 2.1) can be used to de-  
 374 scribe dynamics of a perfect fluid. To take into account influence of viscosity,  
 375 one has to apply the following corrections coming from shear  $\pi^{\mu\nu}$  and bulk  $\Pi$   
 376 viscosities [22]:

$$T^{\mu\nu} = T_0^{\mu\nu} + \pi^{\mu\nu} + \Pi(g^{\mu\nu} - u^\mu u^\nu). \quad (2.3)$$

377 The stress tensor  $\pi^{\mu\nu}$  and the bulk viscosity  $\Pi$  are solutions of dynamical equa-  
 378 tions in the second order viscous hydrodynamic framework [21]. The compari-  
 379 son of hydrodynamics calculations with the experimental results reveal, that the  
 380 shear viscosity divided by entropy  $\eta/s$  has to be small and close to the AdS/CFT  
 381 estimate  $\eta/s = 0.08$  [22, 23]. The bulk viscosity over entropy value used in calcu-  
 382 lations is  $\zeta/s = 0.04$  [22].

383 When using  $T^{\mu\nu}$  to describe system evolving close to local thermodynamic  
 384 equilibrium, relativistic hydrodynamic equations in a form of:

$$\partial_\mu T^{\mu\nu} = 0 \quad (2.4)$$

385 can be used to describe the dynamics of the local energy density, pressure and  
 386 flow velocity.

387 Hydrodynamic calculations are starting from the Glauber<sup>1</sup> model initial con-  
 388 ditions. The collective expansion of a fluid ends at the freeze-out hypersurface.  
 389 That surface is usually defined as a constant temperature surface, or equivalently  
 390 as a cut-off in local energy density. The freeze-out is assumed to occur at the  
 391 temperature  $T = 140$  MeV.

## 392 2.2 Statistical hadronization

393 Statistical description of heavy ion collision has been successfully used  
 394 to describe quantitatively *soft* physics, i.e. the regime with the transverse  
 395 momentum not exceeding 2 GeV. The basic assumption of the statistical  
 396 approach of evolution of the quark-gluon plasma is that at some point of the

---

<sup>1</sup>The Glauber Model is used to calculate “geometrical” parameters of a collision like an impact parameter, number of participating nucleons or number of binary collisions.

space-time evolution of the fireball, the thermal equilibrium is reached. When the system is in the thermal equilibrium the local phase-space densities of particles follow the Fermi-Dirac or Bose-Einstein statistical distributions. At the end of the plasma expansion, the freeze-out occurs. The freeze-out model incorporated in the THERMINATOR model assumes, that chemical and thermal freeze-out occur at the same time.

### 2.2.1 Cooper-Frye formalism

The result of the hydrodynamic calculations is the freeze-out hypersurface  $\Sigma^\mu$ . A three-dimensional element of the surface is defined as [19]

$$d\Sigma_\mu = \epsilon_{\mu\alpha\beta\gamma} \frac{\partial x^\alpha}{\partial \alpha} \frac{\partial x^\beta}{\partial \beta} \frac{\partial x^\gamma}{\partial \gamma} d\alpha d\beta d\gamma, \quad (2.5)$$

where  $\epsilon_{\mu\alpha\beta\gamma}$  is the Levi-Civita tensor and the variables  $\alpha, \beta, \gamma \in \{1, 2, 3\}$  are used to parametrize the three-dimensional freeze-out hypersurface in the Minkowski four-dimensional space. The Levi-Civita tensor is equal to 1 when the indices form an even permutation (eg.  $\epsilon_{0123}$ ), to -1 when the permutation is odd (e.g.  $\epsilon_{2134}$ ) and has a value of 0 if any index is repeated. Therefore [19],

$$d\Sigma_0 = \begin{vmatrix} \frac{\partial x}{\partial \alpha} & \frac{\partial x}{\partial \beta} & \frac{\partial x}{\partial \gamma} \\ \frac{\partial y}{\partial \alpha} & \frac{\partial y}{\partial \beta} & \frac{\partial y}{\partial \gamma} \\ \frac{\partial z}{\partial \alpha} & \frac{\partial z}{\partial \beta} & \frac{\partial z}{\partial \gamma} \end{vmatrix} d\alpha d\beta d\gamma \quad (2.6)$$

and the remaining components are obtained by cyclic permutations of  $t, x, y$  and  $z$ .

One can obtain the number of hadrons produced on the hypersurface  $\Sigma^\mu$  from the Cooper-Frye formalism. The following integral yields the total number of created particles [19]:

$$N = (2s + 1) \int \frac{d^3 p}{(2\pi)^3 E_p} \int d\Sigma_\mu p^\mu f(p_\mu u^\mu), \quad (2.7)$$

where  $f(p_\mu u^\mu)$  is the phase-space distribution of particles (for stable ones and resonances). One can simply derive from Eq. 2.7, the dependence of the momentum density [24]:

$$E \frac{d^3 N}{dp^3} = \int d\Sigma_\mu f(p_\mu u^\mu) p^\mu. \quad (2.8)$$

The momentum distribution  $f$  contains non-equilibrium corrections:

$$f = f_0 + \delta f_{shear} + \delta f_{bulk}, \quad (2.9)$$

where

$$f_0(p_\mu u^\mu) = \left\{ \exp \left[ \frac{p_\mu u^\mu - (B\mu_B + I_3\mu_{I_3} + S\mu_S + C\mu_C)}{T} \right] \pm 1 \right\}^{-1} \quad (2.10)$$

422 In case of fermions, in the Eq. 2.10 there is a plus sign and for bosons, minus  
 423 sign respectively. The thermodynamic quantities appearing in the  $f_0(\cdot)$  are  $T$  -  
 424 temperature,  $\mu_B$  - baryon chemical potential,  $\mu_{I_3}$  - isospin chemical potential,  $\mu_S$   
 425 - strange chemical potential,  $\mu_C$  - charmed chemical potential and the  $s$  is a spin of  
 426 a particle. The hydrodynamic calculations yield the flow velocity at freeze-out as  
 427 well as the stress and bulk viscosity tensors required to calculate non-equilibrium  
 428 corrections to the momentum distribution used in Eq. 2.7. The term coming from  
 429 shear viscosity has a form [22]

$$\delta f_{shear} = f_0(1 \pm f_0) \frac{1}{2T^2(e + p)} p^\mu p^\nu \pi_{\mu\nu} \quad (2.11)$$

430 and bulk viscosity

$$\delta f_{bulk} = C f_0(1 \pm f_0) \left( \frac{(u^\mu p_\mu)^2}{3u^\mu p_\mu} - c_s^2 u^\mu p_\mu \right) \Pi \quad (2.12)$$

431 where  $c_s$  is sound velocity and

$$\frac{1}{C} = \frac{1}{3} \frac{1}{(2\pi)^3} \sum_{hadrons} \int d^3 p \frac{m^2}{E} f_0(1 \pm f_0) \left( \frac{p^2}{3E} - c_s^2 E \right). \quad (2.13)$$

432 The equations presented above are directly used in the THERMINATOR to gen-  
 433 erate the primordial hadrons (created during freeze-out) with the Monte-Carlo  
 434 method. Resonances produced in this way, propagate and decay, in cascades if  
 435 necessary. For every generated particle, its origin point either on a hypersurface  
 436 or is associated with the point of the decay of the parent particle. This informa-  
 437 tion is kept in the simulation due to its importance for the femtoscopic analysis.

438 **Chapter 3**

439 **Particle interferometry**

440 Two-particle interferometry (also called *femtoscopy*) gives a possibility to  
441 investigate space-time characteristics of the particle-emitting source created  
442 in heavy ion collisions. Through the study of particle correlations, their  
443 momentum distributions can be used to obtain information about the spatial  
444 extent of the created system. Using this method, one can measure sizes of the  
445 order of  $10^{-15}$  m and time of the order of  $10^{-23}$  s.

446 **3.1 HBT interferometry**

447 In the 1956 Robert Hanbury Brown and Richard Q. Twiss proposed a  
448 method which through analysis of interference between photons allowed to  
449 investigate angular dimensions of stars. The most important result from the  
450 Hanbury-Brown-Twiss experiments is that two indistinguishable particles can  
451 produce an interference effect. There is almost no difference between normal  
452 interferometry and HBT method, except that the latter one does not take into account  
453 information about phase shift of registered particles. At the beginning  
454 this method was used in astronomy for photon interference, but this effect can  
455 be used also to measure extent of any emitting source. This method was adapted  
456 to heavy ion collisions to investigate dimensions of a system created in those  
457 collisions by studying correlations of identical particles [25]. The main difference  
458 between HBT method in astronomy and femtoscopy is that the first one is based  
459 on space-time HBT correlations and the latter one uses momentum correlations.  
460 The momentum correlations yield the space-time picture of the source, whereas  
461 the space-time HBT correlations provide the characteristic relative momenta of  
462 emitted photons, which gives the angular size of the star without the knowledge  
463 of its radius and lifetime [10].

464 **3.2 Theoretical approach**

465 Intensity interferometry in heavy ion physics uses similar mathematical form-  
 466 alism as the astronomy HBT measurement. Through the measurement of corre-  
 467 lation between particles as a function of their relative momentum one can deduce  
 468 the average separation between emitting sources.

469 **3.2.1 Conventions used**

470 In heavy ion collisions to describe particular directions, components of mo-  
 471 mentum and location of particles, one uses naming convention called the Bertsch-  
 472 Pratt coordinate system. This system is presented in the Fig. 3.1. The three dir-

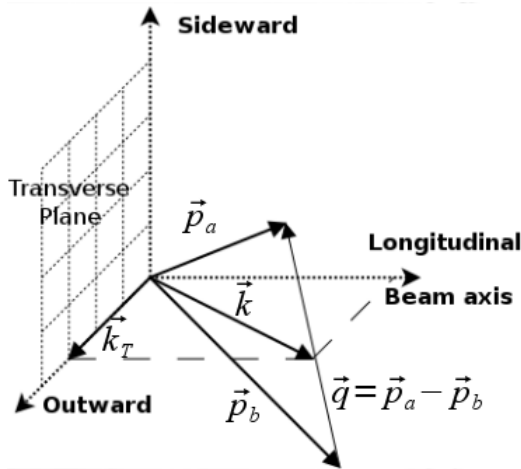


Figure 3.1: Bertsch-Pratt direction naming convention used in heavy ion collision.

472 ections are called *longitudinal*, *outward* and *sideward*. The longitudinal direction  
 473 is parallel to the beam axis. The plane perpendicular to the beam axis is called  
 474 a *transverse plane*. A projection of a particle pair momentum  $\mathbf{k} = (\mathbf{p}_a + \mathbf{p}_b)/2$   
 475 on a transverse plane (a *transverse momentum*  $\mathbf{k}_T$ ) determines *outward* direction:  
 476  $(\mathbf{k})_{out} = \mathbf{k}_T$ . A direction perpendicular to the longitudinal and outward is called  
 477 *sideward*.

478 A particle pair is usually described using two coordinate systems. The first  
 479 one, *Longitudinally Co-Moving System* (**LCMS**) is moving along the particle pair  
 480 with the longitudinal direction, in other words, the pair longitudinal momentum  
 481 vanishes:  $(\mathbf{p}_a)_{long} = -(\mathbf{p}_b)_{long}$ . The second system is called *Pair Rest Frame* (**PRF**).  
 482 In the PRF the centre of mass rests:  $\mathbf{p}_a = -\mathbf{p}_b$ . Variables which are expressed in  
 483 the PRF are marked with a star (e.g.  $\mathbf{k}^*$ ).

484 The transition of space-time coordinates from LCMS to PRF is simply  
 485 a boost along the outward direction, with the transverse velocity of the

pair  $\beta_T = (\mathbf{v}/c)_{out}$  [25]:

$$r_{out}^* = \gamma_t(r_{out} - \beta_T \Delta t) \quad (3.1)$$

$$r_{side}^* = r_{side} \quad (3.2)$$

$$r_{long}^* = r_{long} \quad (3.3)$$

$$\Delta t^* = \gamma_T(\Delta t - \beta_T r_{out}) , \quad (3.4)$$

where  $\gamma_T = (1 - \beta_T^2)^{-1/2}$  is the Lorentz factor. However, in calculations performed in this work the equal time approximation is used, which assumes that particles in a pair were produced at the same time in PRF - the  $\Delta t^*$  is neglected.

The most important variables used to describe particle pair are their total momentum  $\mathbf{P} = \mathbf{p}_a + \mathbf{p}_b$  and relative momentum  $\mathbf{q} = \mathbf{p}_a - \mathbf{p}_b$ . In the PRF one has  $\mathbf{q} = 2\mathbf{k}^*$ , where  $\mathbf{k}^*$  is a momentum of the first particle in PRF.

### 3.2.2 Two particle wave function

Let us consider two identical particles with momenta  $\mathbf{p}_1$  and  $\mathbf{p}_2$  emitted from space points  $\mathbf{x}_1$  and  $\mathbf{x}_2$ . Those emitted particles can be treated as two incoherent waves. If the particles are identical, they are also indistinguishable, therefore one

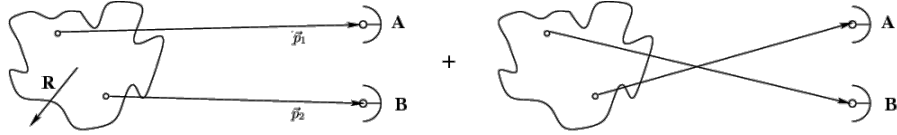


Figure 3.2: The pair wave function is a superposition of all possible states. In case of particle interferometry it includes two cases: particles with momenta  $p_1, p_2$  registered by detectors  $A, B$  and  $p_1, p_2$  registered by  $B, A$  respectively.

has also take into account the scenario, where the particle with momentum  $\mathbf{p}_1$  is emitted from  $\mathbf{x}_2$  and particle  $\mathbf{p}_2$  from  $\mathbf{x}_1$  (Fig. 3.2). In such case, the wave function describing behaviour of a pair has to contain both components [8]:

$$\Psi_{ab}(\mathbf{q}) = \frac{1}{\sqrt{2}} [\exp(-i\mathbf{p}_1\mathbf{x}_1 - i\mathbf{p}_2\mathbf{x}_2) \pm \exp(-i\mathbf{p}_2\mathbf{x}_1 - i\mathbf{p}_1\mathbf{x}_2)] . \quad (3.5)$$

A two particle wave function of identical bosons is symmetric ("+" sign in Eq. 3.5) and in case of identical fermions - antisymmetric ("−" sign). This anti-symmetrization or symmetrization implies the correlation effect coming from the Fermi-Dirac or Bose-Einstein statistics accordingly.

To provide full description of a system consisting of two charged hadrons, one has to include in the wave function besides quantum statistics also Coulomb and strong Final State Interactions. Considering identical particles systems, the quantum statistics is a main source of a correlation. Hence, in case of space-time analysis of particle emitting source, effects coming from the Coulomb and Strong interactions can be neglected.

508    **3.2.3 Source emission function**

509    To describe particle emitting source, one uses a single emission function [25]:

510    
$$S_A(\mathbf{x}_1, \mathbf{p}_1) = \int S(\mathbf{x}_1, \mathbf{p}_1, \mathbf{x}_2, \mathbf{p}_2, \dots, \mathbf{x}_N, \mathbf{p}_N) d\mathbf{x}_2 d\mathbf{p}_2 \dots d\mathbf{x}_N d\mathbf{p}_N \quad (3.6)$$

511    and a two-particle one:

$$S_{AB}(\mathbf{x}_1, \mathbf{p}_1, \mathbf{x}_2, \mathbf{p}_2) = \int S(\mathbf{x}_1, \mathbf{p}_1, \mathbf{x}_2, \mathbf{p}_2, \dots, \mathbf{x}_N, \mathbf{p}_N) d\mathbf{x}_3 d\mathbf{p}_3 \dots d\mathbf{x}_N d\mathbf{p}_N . \quad (3.7)$$

512    Emission function  $S(\cdot)$  can be interpreted as a probability to emit a particle, or  
 513    a pair of particles from a given space-time point with a given momentum. In  
 514    principle, the source emission function should encode all physics aspects of the  
 515    particle emission process i.e. the symmetrization for bosons and fermions, as  
 516    well as the two-body and many body Final State Interactions. Instead of this,  
 517    one assume that each particle's emission process is independent - the interac-  
 518    tion between final-state particles after their creation is independent from their  
 519    emission process. The assumption of this independence allows to construct two-  
 520    particle emission function from single particle emission functions via a convolu-  
 521    tion [25]:

$$S(\mathbf{k}^*, \mathbf{r}^*) = \int S_A(\mathbf{p}_1, \mathbf{x}_1) S_B(\mathbf{p}_2, \mathbf{x}_2) \delta \left[ \mathbf{k}^* - \frac{\mathbf{p}_1 + \mathbf{p}_2}{2} \right] \delta [\mathbf{r}^* - (\mathbf{x}_1 + \mathbf{x}_2)] \times d^4 \mathbf{x}_1 d^4 \mathbf{x}_2 d^4 \mathbf{x}_1 d^3 \mathbf{p}_1 d^3 \mathbf{p}_2 \quad (3.8)$$

522    In case of identical particles, ( $S_A = S_B$ ) several simplifications can be made.  
 523    A convolution of the two same Gaussian distributions is also a Gaussian distri-  
 524    bution with  $\sigma$  multiplied by  $\sqrt{2}$ . Femtoscopy can give information only about  
 525    two-particle emission function, but when considering Gaussian distribution as  
 526    a source function in Eq. 3.8, one can obtain a  $\sigma$  of a single emission function  
 527    from a two-particle emission function. The Eq. 3.8 is not reversible - an inform-  
 528    ation about  $S_A(\cdot)$  cannot be derived from  $S_{AB}(\cdot)$ . An exception from this rule  
 529    is a Gaussian source function, hence it is often used in femtoscopic calculations.  
 530    Considering pairs of identical particles, an emission function is assumed to be  
 531    described by the following equation in the Pair Rest Frame [25]:

$$S_{1D}^{PRF}(\mathbf{r}^*) = \exp \left( -\frac{r_{out}^{*2} + r_{side}^{*2} + r_{long}^{*2}}{4R_{inv}^2} \right) . \quad (3.9)$$

To change from the three-dimensional variables to the one-dimensional variable  
 one requires introduction of the proper Jacobian  $r^{*2}$ .

$$S_{1D}^{PRF}(r^*) = r^{*2} \exp \left( -\frac{r^{*2}}{4R_{inv}^2} \right) . \quad (3.10)$$

532 The “4” in the denominator before the “standard deviation”  $R_{inv}$  in the Gaussian  
 533 distribution comes from the convolution of the two Gaussian distributions,  
 534 which multiplies the  $R_{inv}$  by a factor of  $\sqrt{2}$ .

A more complex form of emission function was used by all RHIC and SPS experiments in identical pion femtoscopy:

$$S_{3D}^{LCMS}(\mathbf{r}) = \exp \left( -\frac{r_{out}^2}{4R_{out}^2} - \frac{r_{side}^2}{4R_{side}^2} - \frac{r_{long}^2}{4R_{long}^2} \right). \quad (3.11)$$

535 The main difference of this source function is that it has three different and inde-  
 536 pendent widths  $R_{out}$ ,  $R_{side}$ ,  $R_{long}$  and they are defined in the LCMS, not in PRF.  
 537 Unlike in PRF, in LCMS an equal-time approximation is not used. For identical  
 538 particles this is not a problem - only Coulomb interaction inside a wave function  
 539 depends on  $\Delta t$ .

#### 540 Relationship between one-dimensional and three-dimensional source sizes

541 Up to now, most of femtoscopic measurements were limited only to averaged  
 542 source size  $R_{av}^L$  (the letter “L” in superscript stands for LCMS):

$$S_{1D}^{LCMS}(\mathbf{r}) = \exp \left( -\frac{r_{out}^2 + r_{side}^2 + r_{long}^2}{2R_{av}^L} \right). \quad (3.12)$$

543 The relationship between between  $S_{1D}^{LCMS}(\cdot)$  and  $S_{3D}^{LCMS}(\cdot)$  is given by:

$$S_{3D}^{LCMS}(r) = \int \exp \left( -\frac{r_{out}^2}{2R_{out}^L} - \frac{r_{side}^2}{2R_{side}^L} - \frac{r_{long}^2}{2R_{long}^L} \right) \times \delta \left( r - \sqrt{r_{out}^2 + r_{side}^2 + r_{long}^2} \right) dr_{out} dr_{side} dr_{long}. \quad (3.13)$$

544 The one-dimensional source size corresponding to the three-dimensional one can  
 545 be approximated by the following form:

$$S_{1D}^{LCMS}(r) = r^2 \exp \left( -\frac{r^2}{2R_{av}^L} \right). \quad (3.14)$$

546 The equation above assumes that  $R_{out}^L = R_{side}^L = R_{long}^L$  hence  $R_{av}^L = R_{out}^L$ . If this  
 547 condition is not satisfied, one can not give explicit mathematical relation between  
 548 one-dimensional and three-dimensional source sizes. However, for realistic val-  
 549 ues of  $R$  (i.e. for similar values of  $R_{out}$ ,  $R_{side}$ ,  $R_{long}$ ), the  $S_{3D}^{LCMS}$  from Eq. 3.13 is  
 550 not very different from Gaussian distribution and can be well approximated by  
 551 Eq. 3.13.

552 A deformation of an averaged source function in case of big differences in  
 553  $R_{out}$ ,  $R_{side}$ ,  $R_{long}$  is presented in the Fig. 3.3. A three-dimensional Gaussian dis-  
 554 tribution with varying widths was averaged into one-dimensional function using

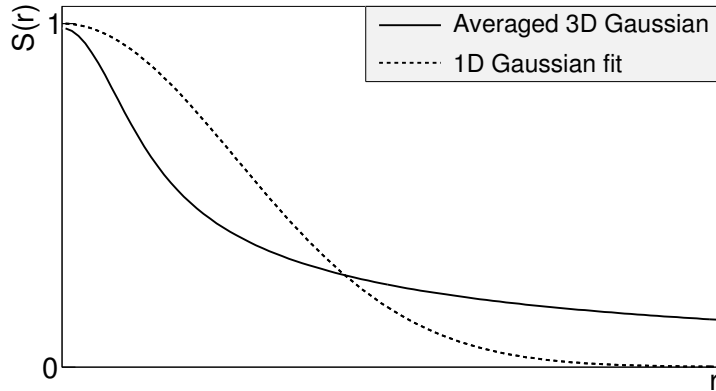


Figure 3.3: An averaged three-dimensional Gaussian source function with different widths was averaged into one-dimensional function. To illustrate deformations, one-dimensional Gaussian distribution was fitted.

the Eq. 3.13. Afterwards, an one-dimensional Gaussian distribution was fitted.  
One can notice a heavy tail of an averaged distribution in long  $r$  region, which  
makes an approximation using one-dimensional distribution in this case quite  
inaccurate.

Using Eq. 3.13 and Eq. 3.14 one can obtain a relation between one-dimensional width and the three-dimensional ones. Through numerical calculations one can find the following approximate relation [25]:

$$R_{av}^L = \sqrt{\left(R_{out}^L\right)^2 + \left(R_{side}^L\right)^2 + \left(R_{long}^L\right)^2} / 3 . \quad (3.15)$$

This equation does not depend on the pair velocity, hence it is valid in the LCMS and PRF.

### 3.2.4 Theoretical correlation function

The fundamental object in a particle interferometry is a correlation function.  
The correlation function is defined as:

$$C(\mathbf{p}_a, \mathbf{p}_b) = \frac{P_2(\mathbf{p}_a, \mathbf{p}_b)}{P_1(\mathbf{p}_a)P_1(\mathbf{p}_b)} , \quad (3.16)$$

where  $P_2$  is a conditional probability to observe a particle with momentum  $\mathbf{p}_b$  if particle with momentum  $\mathbf{p}_a$  was also observed. A  $P_1$  is a probability to observe a particle with a given momentum. The relationship between source emission function, pair wave function and the correlation function is described by the following equation:

$$C(\mathbf{p}_1, \mathbf{p}_2) = \int S_{AB}(\mathbf{p}_1, \mathbf{x}_1, \mathbf{p}_2, \mathbf{x}_2) |\Psi_{AB}|^2 d^4\mathbf{x}_1 d^4\mathbf{x}_2 \quad (3.17)$$

Substituting the one-dimensional emission function (Eq. 3.10) into the integral above yields the following form of correlation function in PRF:

$$C(q) = 1 + \lambda \exp(-R_{inv}^2 q^2) \quad (3.18)$$

where  $q$  is a momentum difference between two particles. When using the three-dimensional emission function (Eq. 3.11) one gets the following correlation function defined in the LCMS:

$$C(\mathbf{q}) = 1 + \lambda \exp(-R_{out}^2 q_{out}^2 - R_{side}^2 q_{side}^2 - R_{long}^2 q_{long}^2) \quad (3.19)$$

569 where  $q_{out}$ ,  $q_{side}$ ,  $q_{long}$  are  $\mathbf{q}$  components in the outward, sideward and longitudinal direction. The  $\lambda$  parameter in the equations above determines correlation  
 570 strength. The lambda parameter has values in the range  $\lambda \in [-0.5, 1]$  and it depends on a pair type. In case of pairs of identical bosons (like  $\pi\pi$  or  $KK$ ) the  
 571 lambda parameter  $\lambda \rightarrow 1$ . For identical fermions (e.g.  $p-p$ )  $\lambda \rightarrow -0.5$ . Values of  
 572  $\lambda$  observed experimentally are lower than 1 (for bosons) and greater than -0.5  
 573 (for fermions). There are few explanations to this effect: detector efficiencies,  
 574 inclusion of misidentified particles in a used sample or inclusion of non-correlated  
 575 pairs (when one or both particles come from e.g. long-lived resonance). The  
 576 analysis carried out in this work uses data from a model, therefore the detector  
 577 efficiency and particle purity is not taken into account [25].  
 578

### 580 3.2.5 Spherical harmonics decomposition of a correlation function

581 Results coming from an analysis using three-dimensional correlation function  
 582 in Cartesian coordinates are quite difficult to visualize. To do that, one usually  
 583 performs a projection into a one dimension in outward, sideward and longitudinal  
 584 directions. One may loose important information about a correlation  
 585 function in this procedure, because it gives only a limited view of the full three-  
 586 dimensional structure. Recently, a more advanced way of presenting correlation  
 587 function - a spherical harmonics decomposition, was proposed. The three-  
 588 dimensional correlation function is decomposed into an infinite set of components  
 589 in a form of one-dimensional histograms  $C_l^m(q)$ . In this form, a correlation  
 590 function is defined as a sum of a series [26]:

$$C(\mathbf{q}) = \sum_{l,m} C_l^m(q) Y_l^m(\theta, \phi), \quad (3.20)$$

591 where  $Y_l^m(\theta, \phi)$  is a spherical harmonic function. Spherical harmonics are an  
 592 orthogonal set of solutions to the Laplace's equation in spherical coordinates  
 593 Hence, in this approach, a correlation function is defined as a function of  $q$ ,  $\theta$   
 594 and  $\phi$ . To obtain  $C_l^m$  coefficients in the series, one has to calculate the following  
 595 integral:

$$C_l^m(q) = \int_{\Omega} C(q, \theta, \phi) Y_l^m(\theta, \phi) d\Omega, \quad (3.21)$$

596 where  $\Omega$  is a full solid angle.

Spherical harmonics representation has several important advantages. The main advantage of this decomposition is that it requires less statistics than traditional analysis performed in Cartesian coordinates. Another one is that it encodes full three-dimensional information in a set of one-dimensional plots. In principle it does not have to be an advantage, because full description of a correlation function requires infinite number of  $l, m$  components. But it so happens that the intrinsic symmetries of a pair distribution in a femtoscopic analysis result in most of the components to vanish. For the identical particles correlation functions, all coefficients with odd values of  $l$  and  $m$  disappear. It has also been shown, that the most significant portion of femtoscopic data is stored in the components with the lowest  $l$  values. It is expected that, the main femtoscopic information is contained in the following components [25]:

$$C_0^0 \rightarrow R_{LCMS}, \quad (3.22)$$

$$\Re C_2^0 \rightarrow \frac{R_T}{R_{long}}, \quad (3.23)$$

$$\Re C_2^2 \rightarrow \frac{R_{out}}{R_{side}}, \quad (3.24)$$

597 where  $R_{LCMS} = \sqrt{(R_{out}^2 + R_{side}^2 + R_{long}^2)/3}$  and  $R_T = \sqrt{(R_{out}^2 + R_{side}^2)/2}$ .  
 598 The  $C_0^0$  is sensitive to the overall size of a correlation function. The  $\Re C_2^0$  carries  
 599 the information about the ratio of the transverse to the longitudinal radii, due  
 600 to its  $\cos^2(\theta)$  weighting in  $Y_2^0$ . The component  $\Re C_2^2$  with its  $\cos^2(\phi)$  weighting  
 601 encodes the ratio between outward and sideward radii. Thus, the spherical har-  
 602 monics method allows to obtain and analyze full three-dimensional femtoscopic  
 603 information from a correlation function [25].

### 604 3.3 Experimental approach

605 The correlation function is defined as a probability to observe two particles  
 606 together divided by the product of probabilities to observe each of them sepa-  
 607 rately (Eq. 3.16). Experimentally this is achieved by dividing two distributions  
 608 of relative momentum of pairs of particles coming from the same event and the  
 609 equivalent distribution of pairs where each particle is taken from different colli-  
 610 sions. In this way, one obtains not only femtoscopic information but also all other  
 611 event-wide correlations. This method is useful for experimentalists to estimate  
 612 the magnitude of non-femtoscopic effects. There exists also a different approach,  
 613 where two particles in pairs in the second distribution are also taken from the  
 614 same event. The second method gives only information about physical effects  
 615 accessible via femtoscopy. The aim of this work is a study of effects coming from  
 616 two particle interferometry, hence the latter method was used.

617 In order to calculate experimental correlation function, one uses the follow-  
 618 ing approach. One has to construct two histograms: the *numerator*  $N$  and the

619 denominator  $D$  with the particle pairs momenta, where particles are coming from  
 620 the same event. Those histograms can be one-dimensional (as a function of  $|\mathbf{q}|$ ),  
 621 three dimensional (a function of three components of  $\mathbf{q}$  in LCMS) or a set of one-  
 622 dimensional histogram representing components of the spherical harmonic de-  
 623 composition of the distribution. The second histogram,  $D$  is filled for each pair  
 624 with the weight 1.0 at a corresponding relative momentum  $\mathbf{q} = 2\mathbf{k}^*$ . The first one,  
 625  $N$  is filled with the same procedure, but the weight is calculated as  $|\Psi_{ab}(\mathbf{r}^*, \mathbf{k}^*)|^2$ .  
 626 A division  $N/D$  gives the correlation function  $C$ . This procedure can be simply  
 627 written as [25]:

$$C(\mathbf{k}^*) = \frac{N}{D} = \frac{\sum_{n_i \in D} \delta(\mathbf{k}^* i - \mathbf{k}^*) |\Psi_{ab}(\mathbf{r}^* i, \mathbf{k}^* i)|^2}{\sum_{n_i \in D} \delta(\mathbf{k}^* i - \mathbf{k}^*)} . \quad (3.25)$$

The  $D$  histogram represents the set of all particle pairs used in calculations.  
 The  $n_i$  is a pair with the its relative momentum  $\mathbf{k}^* i$  and relative separation  $\mathbf{r}^* i$ .  
 The wave function used in Eq. 3.25 has one of the following forms:

$$|\Psi_{\pi\pi}(\mathbf{r}^*, \mathbf{k}^*)|^2 = |\Psi_{KK}(\mathbf{r}^*, \mathbf{k}^*)|^2 = 1 + \cos(2\mathbf{k}^*\mathbf{r}^*) , \quad (3.26)$$

$$|\Psi_{pp}(\mathbf{r}^*, \mathbf{k}^*)|^2 = 1 - \frac{1}{2} \cos(2\mathbf{k}^*\mathbf{r}^*) . \quad (3.27)$$

628 The first one is used in case of bosons, and the latter one is for identical fermi-  
 629 ons. Mathematically, the procedure of calculating the Eq. 3.25 is equivalent to a  
 630 calculation of an integral in Eq. 3.17 through a Monte-Carlo method.

### 631 3.4 Scaling of femtoscopic radii

632 In the hydrodynamic models describing expansion of a quark-gluon plasma,  
 633 particles are emitted from the source elements. Each of the source elements is  
 634 moving with the velocity  $u_\mu$  given by hydrodynamic equations. Because solu-  
 635 tions of those equations are smooth, nearby source elements have similar velo-  
 636 cities. Each emitted particle from a certain source element is boosted with the  
 637 flow velocity  $u_\mu$  according to the point of origin. Hence particles emitted close  
 638 to each other (pairs with large transverse momentum  $|\mathbf{k}_T|$ ) will gain the similar  
 639 velocity boost, they can combine into pairs with small relative momenta ( $|\mathbf{q}|$ ) and  
 640 therefore become correlated. If the two particles are emitted far away from each  
 641 other (a pair with small  $|\mathbf{k}_T|$ ), the flow field  $u_\mu$  in their point of emission might  
 642 be very different and it will be impossible for them to have sufficiently small rel-  
 643 ative momenta in order to be in region of interference effect. This effect is visible  
 644 in a width of a correlation function in the Fig. 3.4. The correlation function gets  
 645 broader for greater values of  $|\mathbf{k}_T|$  and the femtoscopic radius  $R$  becomes smal-  
 646 ler [8, 27].

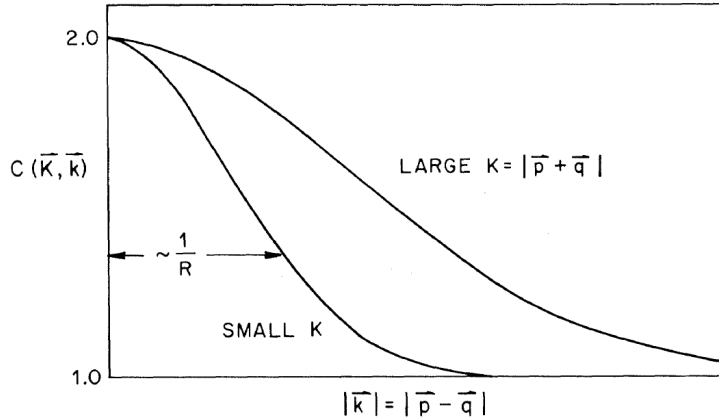


Figure 3.4: Correlation function width dependence on total pair momentum. Pion pairs with a large total momentum are more correlated [27].

#### 647 3.4.1 Scaling in LCMS

Hydrodynamic calculations performed in LCMS show that femtoscopic radii in outward, sideward, and longitudinal direction show dependence on transverse mass  $m_T = \sqrt{k_T^2 + m^2}$ , where  $m$  is a mass of a particle [28]. Moreover, experimental results show that this scaling is observed for  $R_{LCMS}$  radii also. This dependence can be expressed as follows:

$$R_i = \alpha m_T^{-\beta} \quad (3.28)$$

648 where  $i$  subscript indicates that this equation applies to  $R_{out}$ ,  $R_{side}$  and  $R_{long}$   
 649 radii. The  $\beta$  exponent is approximately equal 0.5. In case of strong transversal  
 650 expansion of the emitting source, the decrease of longitudinal interferometry ra-  
 651 dius can be more quick than  $m_T^{-0.5}$ , hence one can expect for longitudinal radii  
 652 greater values of  $\beta > 0.5$  [28].

#### 653 3.4.2 Scaling in PRF

654 In the collisions at the LHC energies, pions are most abundant particles and  
 655 their multiplicities are large enough to enable three-dimensional analysis. How-  
 656 ever, for heavier particles, such as kaons and protons statistical limitations arise.  
 657 Hence it is often possible to only measure one-dimensional radius  $R_{inv}$  for those  
 658 particles. The  $R_{inv}$  is then calculated in the PRF. The transition from LCMS to  
 659 PRF is a Lorentz boost in the direction of pair transverse momentum with velo-  
 660 city  $\beta_T = p_T/m_T$ . Hence only  $R_{out}$  radius changes:

$$R_{out}^* = \gamma_T R_{out}. \quad (3.29)$$

661 The one-dimensional  $R_{inv}$  radius is direction-averaged source size in PRF. One  
 662 can notice, that such power-law scaling of  $R_{inv}$  described by Eq. 3.28 is not

663 observed. To recover such scaling in PRF one has to take into consideration two  
 664 effects when transforming variables from LCMS to PRF: overall radius growths  
 665 and source distribution becomes non-Gaussian, while developing long-range  
 666 tails (see Fig. 3.3 for an example). The interplay of these two effects can be  
 667 accounted with an approximate formula:

$$R_{inv} = \sqrt{(R_{out}^2 \sqrt{\gamma_T} + R_{side}^2 + R_{long}^2)/3} . \quad (3.30)$$

Assuming that all radii are equal  $R_{out} = R_{side} = R_{long}$  this formula can be simplified:

$$R_{LCMS} \approx R_{inv} \times [(\sqrt{\gamma_T} + 2)/3]^{-1/2} . \quad (3.31)$$

668 This approximate formula allows to restore power-law behaviour of the scaled  
 669 radii not only when the radii are equal, but also when their differences are small  
 670 (for explanation see the last part of the section 3.2.3).

671 This method of recovering scaling in PRF can be used as a tool for the search  
 672 of hydrodynamic collectivity between pions, kaons and protons in heavy ion col-  
 673 lisions with the measurement of one-dimensional radius in PRF.

674 **Chapter 4**

675 **Results**

676 For the purposes of the femtoscopy analysis in this thesis, the THERMINATOR  
677 model was used to generate large number of events for eight different sets of  
678 initial conditions corresponding the following centrality ranges: 0-5%, 0-10%, 10-  
679 20%, 20-30%, 30-40%, 40-50%, 50-60% and 60-70% for the Pb-Pb collisions at the  
680 centre of mass energy  $\sqrt{s_{NN}} = 2.76$  TeV.

681 **4.1 Identical particles correlations**

682 The correlation functions (three-dimensional and one-dimensional) were cal-  
683 culated separately for the following different pairs of identical particles:  $\pi-\pi$ ,  $K-$   
684  $K$  and  $p-p$  for nine  $k_T$  bins (in GeV/c): 0.1-0.2, 0.2-0.3, 0.3-0.4, 0.4-0.5, 0.6-0.7,  
685 0.7-0.8, 0.8-1.0 and 1.0-1.2. In case of kaons,  $k_T$  ranges start from 0.3 and for pi-  
686 ons from 0.4 and for both of them the maximum value is 1.0. The  $k_T$  ranges for  
687 the heavier particles were limited to maintain sufficient multiplicity to perform  
688 reliable calculations.

689 **4.1.1 Spherical harmonics components**

690 The three-dimensional correlation function as a function of relative  
691 momentum  $q_{LCMS}$  was calculated in a form of components of spherical  
692 harmonics series accordingly to the Eq. 3.21. In the femtoscopy analysis of  
693 identical particles, the most important information is stored in the  $\Re C_0^0$ ,  $\Re C_2^0$   
694 and  $\Re C_2^2$ , hence only those components were analyzed. Correlation functions  
695 obtained in this procedure were calculated for the different centrality bins for the  
696 pairs of pions, kaons and protons. They are presented in the Fig. 4.1, 4.2 and 4.3.

697 Coefficients for pairs of identical bosons (pions and kaons) are shown in the  
698 Fig. 4.1 and 4.2. The wave function symmetrization (Bose-Einstein statistics)  
699 causes the increase of a correlation in the low relative momenta regime ( $q_{LCMS} <$   
700 0.06 GeV/c or even  $q_{LCMS} < 0.12$  GeV/c for more peripheral collisions). It is  
701 clearly visible in the  $\Re C_0^0$  component. The  $\Re C_0^0$  resembles one-dimensional cor-

relation function and in fact it encodes information about overall source radius. The second coefficient  $\Re C_2^0$  differs from zero (is negative), which yields the information about the ratio  $R_T/R_{long}$ . The  $\Re C_2^2$  stores the  $R_{out}/R_{side}$  ratio and one can notice that is non-vanishing (is also negative).

The correlation function for a pair of identical fermions is presented in the Fig. 4.3. An influence of wave function anti-symmetrization (Fermi-Dirac statistics) has its effect in the decrease of a correlation down to 0.5 at low relative momentum ( $q_{LCMS} < 0.1 \text{ GeV/c}$  or  $q_{LCMS} < 0.15 \text{ GeV/c}$  for more peripheral collisions), which can be observed in  $\Re C_0^0$ . The  $\Re C_2^0$  and  $\Re C_2^2$  coefficients differ from zero and are becoming positive.

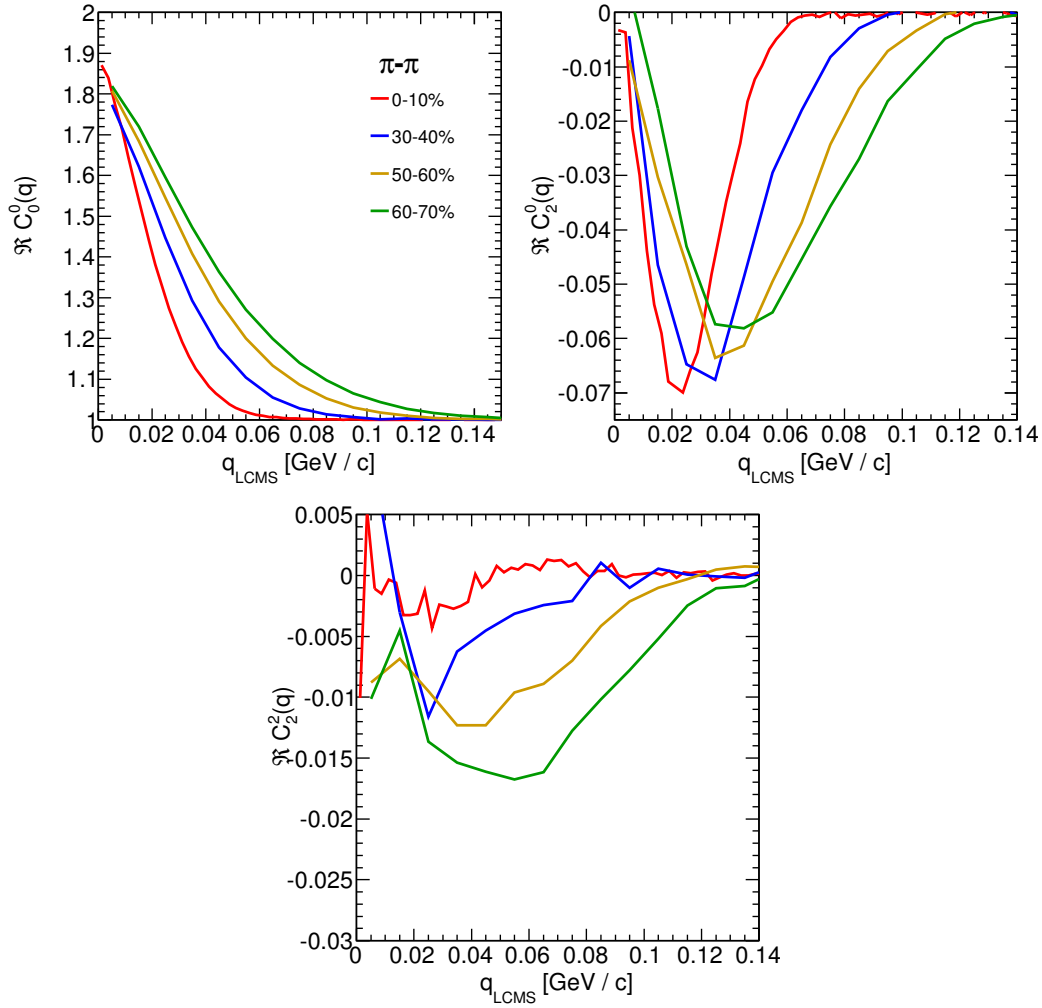


Figure 4.1: Spherical harmonics coefficients of the two-pion correlation function. From the top left:  $\Re C_0^0$ ,  $\Re C_2^0$  and  $\Re C_2^2$ . Only few centrality bins are presented for increased readability.

The common effect of the spherical harmonics form of a correlation function is the “mirroring” of the shape of the  $\Re C_0^0$  coefficient - when correlation function increases at low  $q_{LCMS}$ , the  $\Re C_2^0$  and  $\Re C_2^2$  are becoming negative and vice versa. This is quite different behaviour than in the case of correlations of non-identical particles, where the  $\Re C_2^0$  still behaves in the same manner, but  $\Re C_2^2$  has the opposite sign to the  $\Re C_2^0$  [25].

In all cases, the correlation function gets wider with the peripherality of a collision i.e. the correlation function for most central collisions (0-10%) is much narrower than for the most peripheral ones (60-70%). This phenomena in clearly

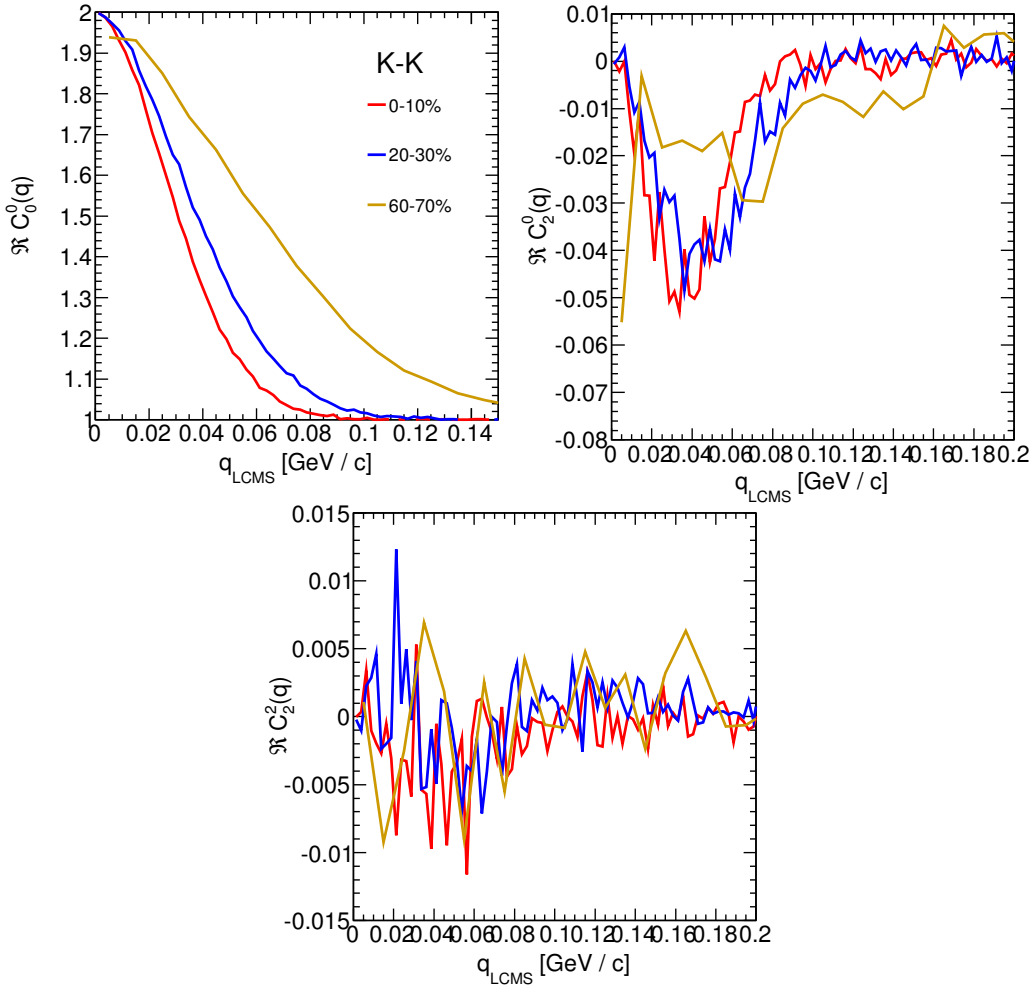


Figure 4.2: Spherical harmonics coefficients of the two-kaon correlation function. From the top left:  $\Re C_0^0$ ,  $\Re C_2^0$  and  $\Re C_2^2$ . Only few centrality bins are presented for increased readability. The  $\Re C_2^2$  is noisy, but one can still notice that it differs from zero and is becoming negative.

visible the  $\Re C_0^0$  coefficients. Other components are also affected by this effect, this is especially noticeable in the case of kaons and pions. For the protons, the results are noisy, hence this effect is not clearly distinguishable.

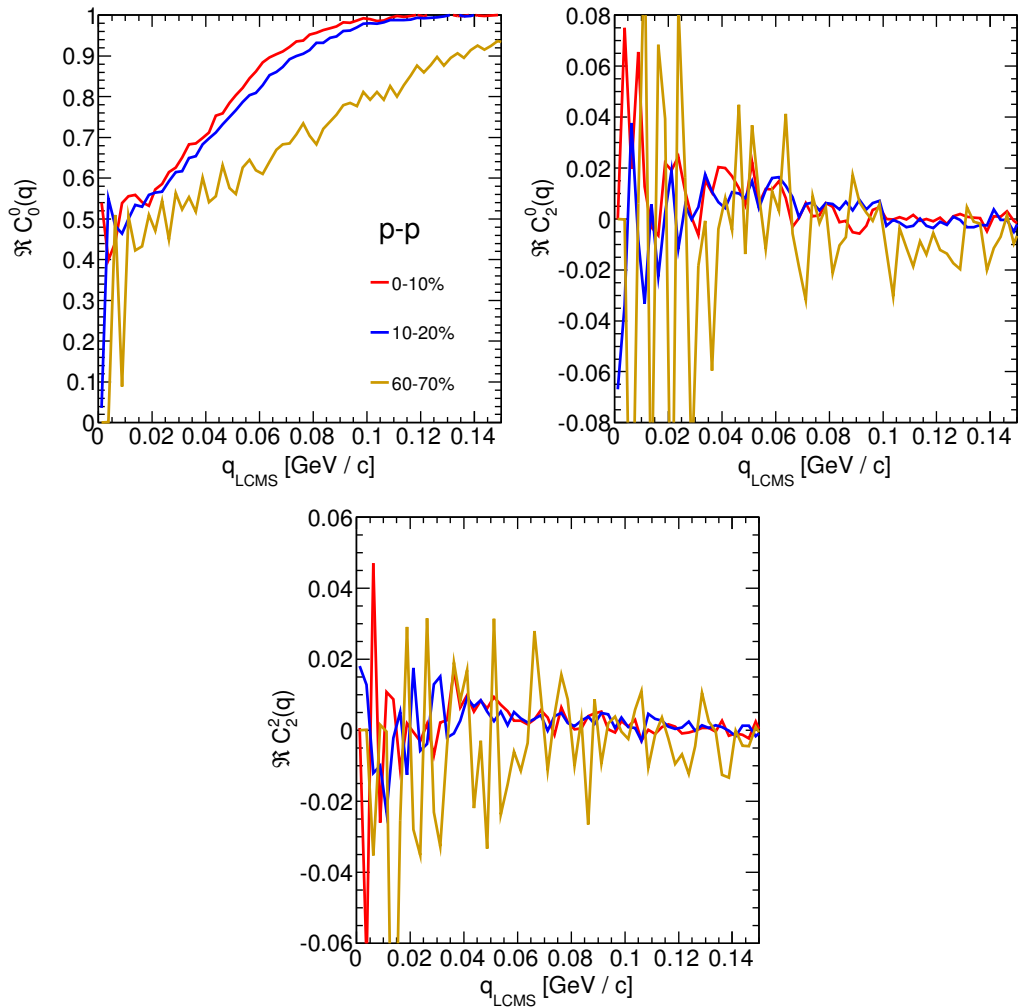


Figure 4.3: Spherical harmonics coefficients of the two-proton correlation function. From the top left:  $\Re C_0^0$ ,  $\Re C_2^0$  and  $\Re C_2^2$ . Only few centrality bins are presented for increased readability. The  $\Re C_2^0$  and  $\Re C_2^2$  are noisy, but one can still notice, that they differ from zero and are becoming positive.

724 **4.1.2 Centrality dependence of a correlation function**

725 The centrality dependence of a correlation function is especially visible in  
 726 one-dimensional correlation functions. This effect is presented in the Fig. 4.4 -  
 727 the correlation functions for pions, kaons and protons are plotted for the same  
 728  $k_T$  range but different centrality bins. One can notice that the width of a func-  
 729 tion is smaller in the case of most central collisions. Hence, the femtoscopic radii  
 730 (proportional to the inverse of width) are increasing with the centrality. An ex-  
 731 planation for this growth is that in the most central collisions, a size of a created  
 system is larger than for the peripheral ones.

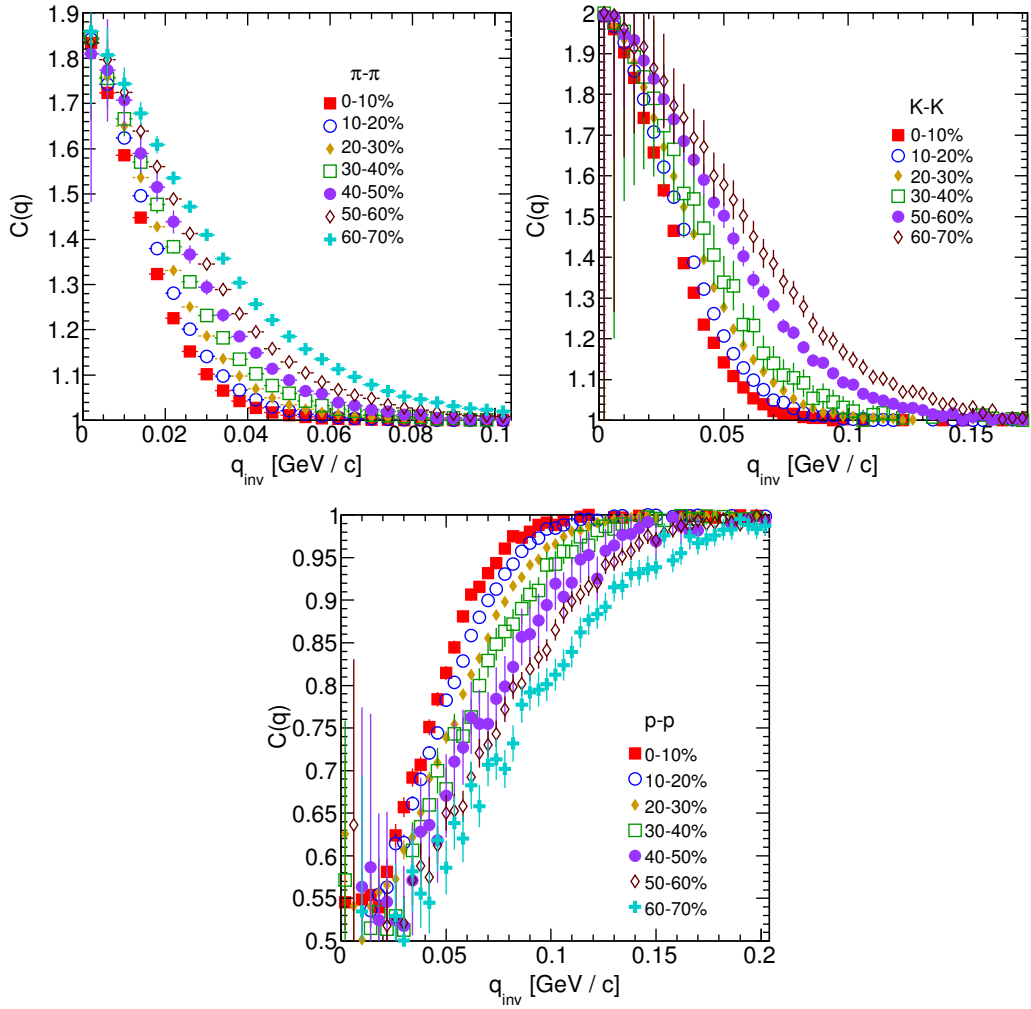


Figure 4.4: One-dimensional correlation function for pions (top left), kaons (top right) and protons (bottom) for different centralities.

733 **4.1.3  $k_T$  dependence of a correlation function**

734 In the Fig. 4.5 there are presented one-dimensional correlation functions for  
 735 pions, kaons and protons for the same centrality bin, but different  $k_T$  ranges. One  
 736 can observe in all cases of the particle types, appearance of the same trend: with  
 737 the increase of the total transverse momentum of a pair, the width of a correlation  
 738 function increases and the femtoscopic radius decreases. The plots in the Fig. 4.5  
 739 were zoomed in to show the influence of  $k_T$ .

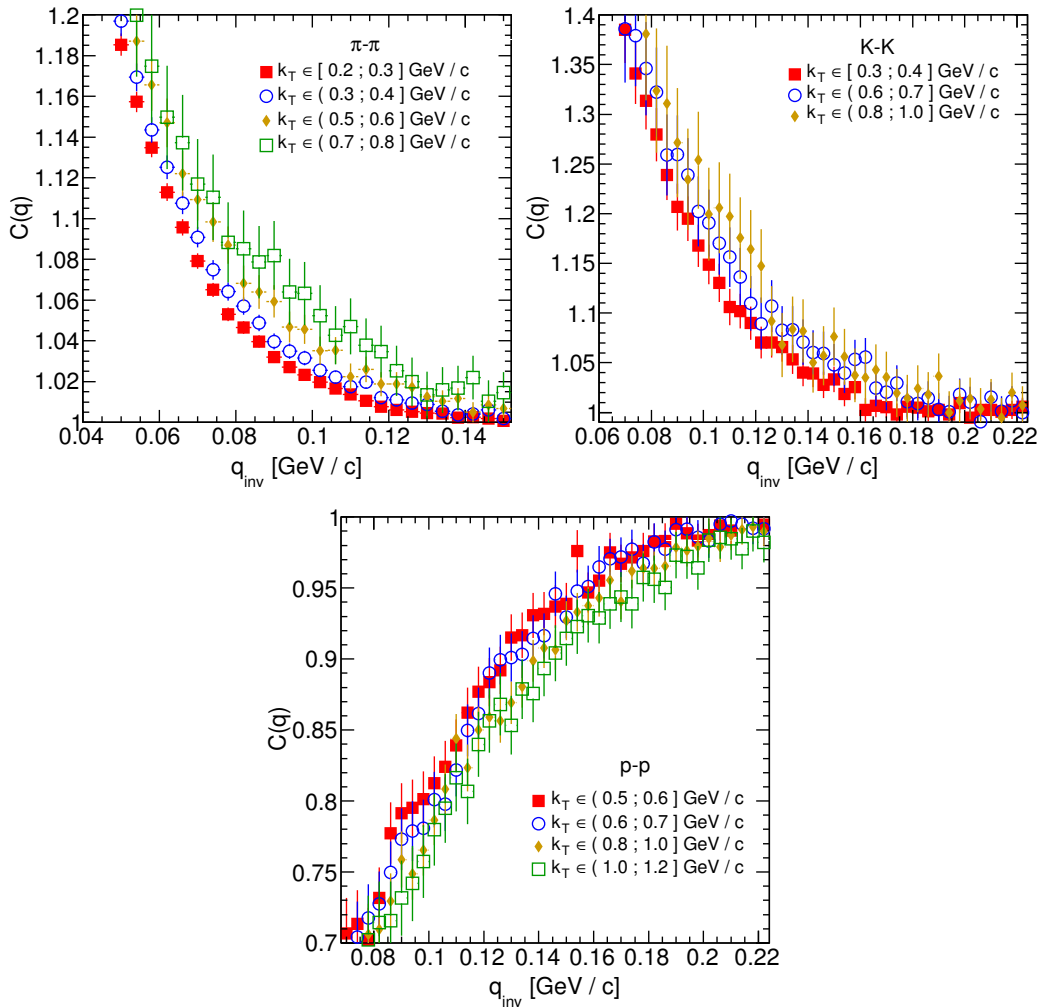


Figure 4.5: One-dimensional correlation functions for pions, kaons and protons, for the same centrality bin and different  $k_T$  ranges. The plot was zoomed in to the region which illustrates the  $k_T$  dependence in the best way. Only few of the calculated ranges are presented for better readability.

## 740 4.2 Results of the fitting procedure

741 In order to perform a quantitative analysis of a wide range of correlation  
 742 functions, the theoretical formulas were fitted to the calculated experimental-  
 743 like data. In this procedure, the femtoscopic radii for the three-dimensional as  
 744 well as one-dimensional correlation functions were extracted. The main goal of  
 745 this analysis is a verification of a common transverse mass scaling for different  
 746 particles types. Obtained radii are plotted as a function of a transverse mass  
 747  $m_T = \sqrt{k_T^2 + m^2}$ . To test the scaling, the following power-law was fitted to the  
 748 particular radii afterwards:

$$R_x = \alpha m_T^{-\beta}, \quad (4.1)$$

749 where the  $\alpha$  and  $\beta$  are free parameters.

### 750 4.2.1 The three-dimensional femtoscopic radii scaling

751 In the Fig. 4.6 there are presented femtoscopic radii in the outward, sideward  
 752 and longitudinal directions for the analysis of two-pion correlation functions in

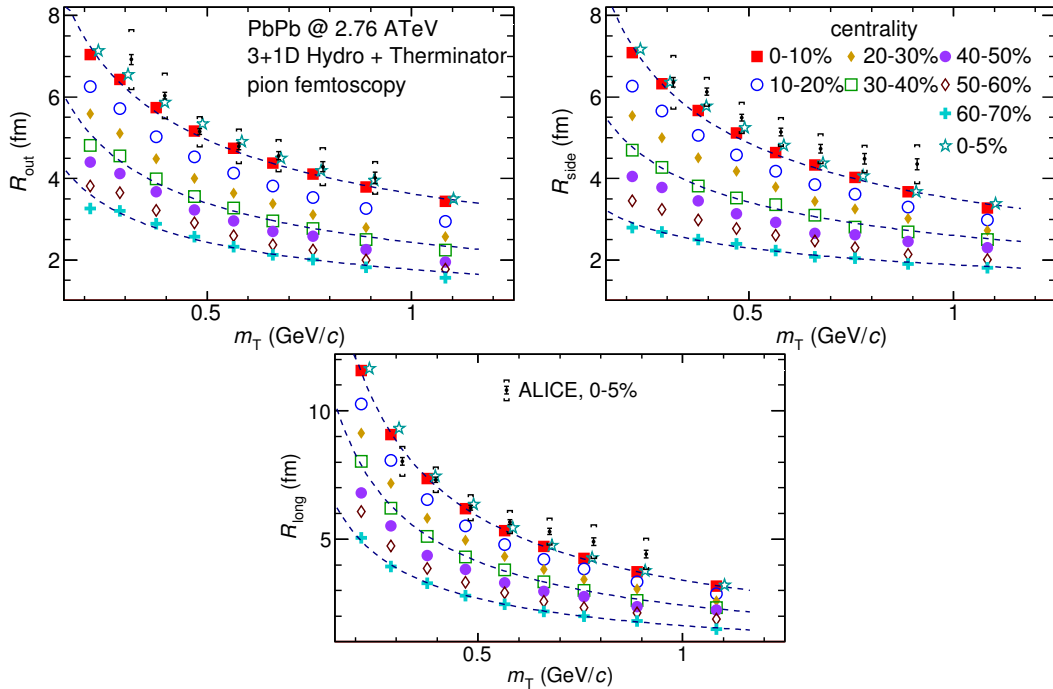


Figure 4.6: Femtoscopic radii in LCMS coming from two-pion correlation functions for all centrality bins as a function of  $m_T$ . The dashed lines are power-law fits. The most central collisions (0-5%) are compared to the results from ALICE [29]. The two datasets are shifted to the right for visibility [30].

the LCMS. The dashed lines are fits of the power law to the data. One can notice, that the power law describes well data points with a 5% accuracy. The  $\beta$  fit parameter for the outward direction is in the order of 0.45. For the sideward direction, this parameter has the similar value, but it is lower for the most peripheral collisions. In case of the longitudinal direction, the  $\beta$  has greater value, up to 0.75. In the Fig. 4.6 there are also compared results for the top 5% central collisions (star-shaped markers) with experimental data from ALICE [29]. The experimental results are consistent with the ones coming from the model predictions.

The Fig. 4.7 presents femtoscopic radii coming from the kaon calculations. The  $R_{out}$ ,  $R_{side}$  and  $R_{long}$  fall also with the power-law within the 5% accuracy. The  $\beta$  parameter was larger in case of kaons: 0.59 in outward direction, 0.54 in the sideward and 0.86 for longitudinal.

The results for two-proton analysis are shown in the Fig. 4.8. The Eq. 4.1 was fitted to the data and tells that the protons also follow the  $m_T$  scaling within 5% range. The  $\beta$  parameter values were even bigger for the outward ( 0.58 ), sideward ( 0.61 ) and longitudinal ( 1.09 ) directions than for the other particle types.

The Fig. 4.9 presents results for the pions, kaons and protons together as a function of  $m_T$ . Considering differences in the  $\beta$  value for the fits for differ-

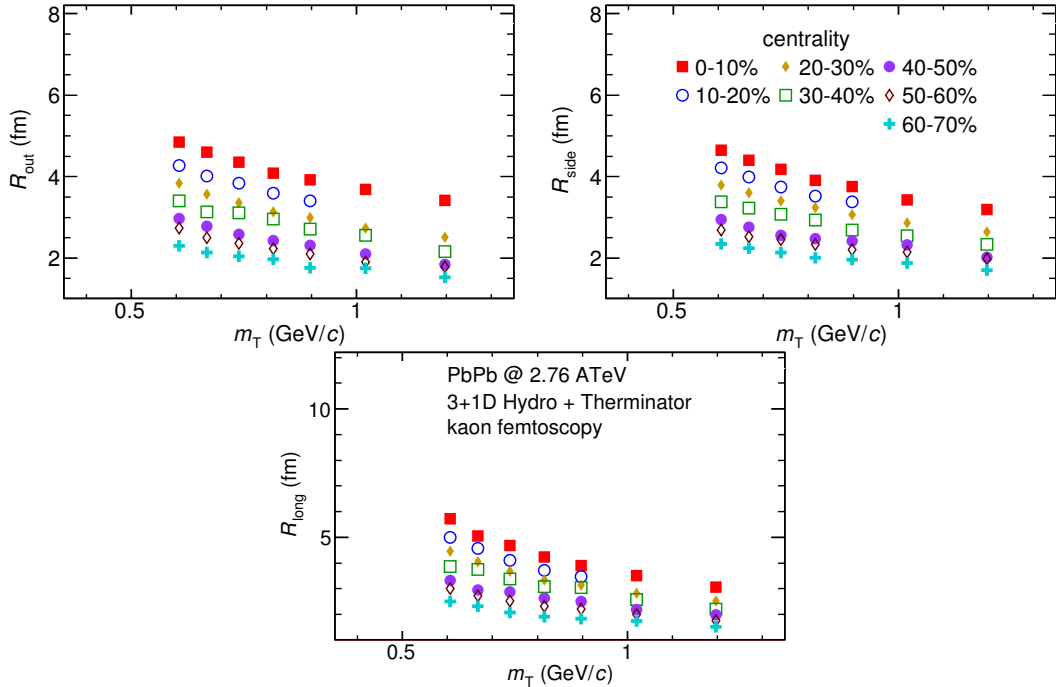


Figure 4.7: Femtoscopic radii extracted from two-kaon correlation functions for different centrality bins as a function of  $m_T$ . [30].

ent particles, one can suspect that there is no common scaling between different kinds of particles. However, when all of the results shown on the same plot, they are aligning on the common curve and the scaling is well preserved. The scaling accuracy is 3%, 5% and 4% for the 0-10%, 20-30% and 60-70% for the outward direction. For the sideward radii the scaling is better, with average deviations 2%, 2% and 3% respectively. In case of longitudinal direction the accuracy is 6%, 5% and 3% for the three centralities. The  $\beta$  parameter for the outward direction is close to the 0.42 in all cases. For the sideward direction it varies from 0.28 to 0.47 and is bigger for more central collisions. Regarding longitudinal radii, the exponent is bigger than the other two:  $\beta \in [0.62; 0.72]$ . Considering all results, the plotted radii are following the common power-law scaling within the 5% accuracy for all directions, centralities and particle types.

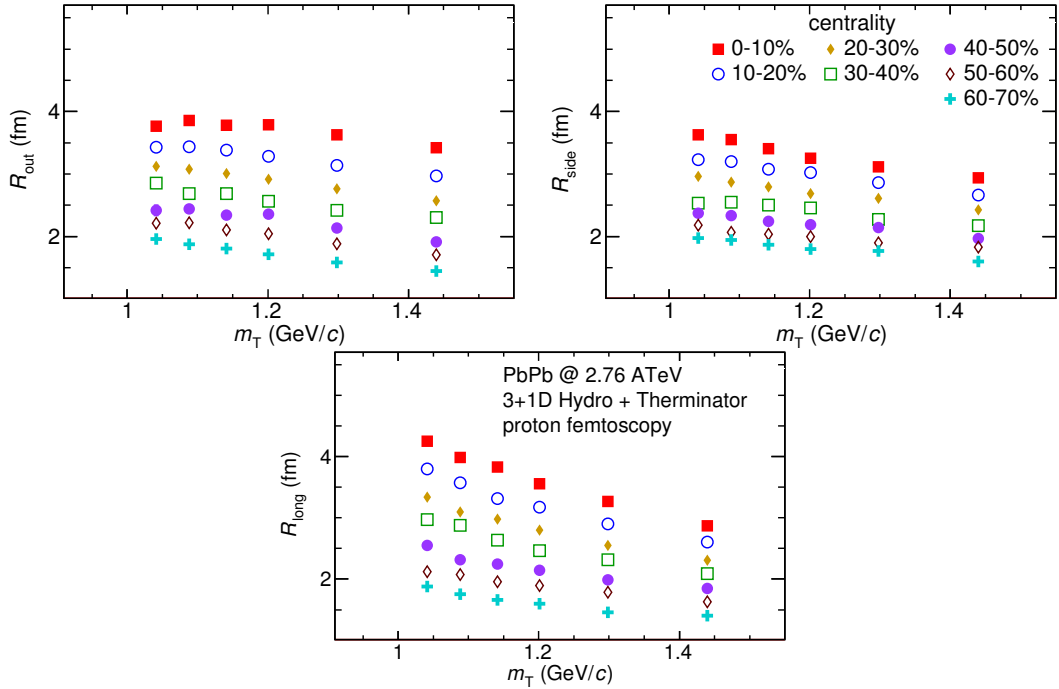


Figure 4.8: Femtoscopic radii extracted from two-proton correlation functions for different centrality bins as a function of  $m_T$ . [30].

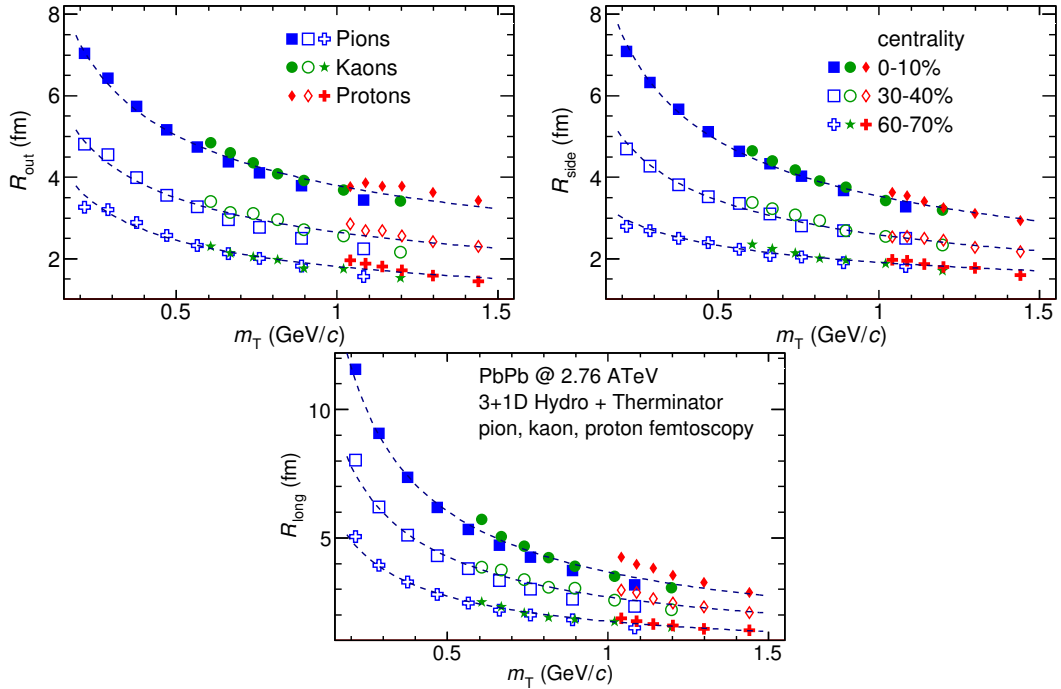


Figure 4.9: The results from the calculations for the pions, kaons and protons in for the three centralities presented on the common plot. One can notice that radii for particular centralities and different particle types follow the common power-law scaling. [30].

785 **4.2.2 Scaling of one-dimensional radii**

786 To the one-dimensional correlation function, the corresponding function in  
 787 the PRF given by the Eq. 3.18 was fitted. The results from those fits are presented  
 788 in the upper left plot in the Fig. 4.10. One immediately notices, that there is no  
 789 common scaling of  $R_{inv}$  for different kind of particles. In the Fig. 4.9 the radii  
 790 in the outward direction for the pions, kaons and protons for the same  $m_T$  are  
 791 similar. However, when one performs a transition from the LCMS to the PRF, the  
 792  $R_{out}$  radius grows:

$$R_{out}^* = \gamma_T R_{out}, \quad (4.2)$$

793 where  $\gamma_T = m_T/m$ . For the lighter particles, the  $\gamma_T$  is much larger, hence the  
 794 bigger growth of the  $R_{out}$  and the overall radius. This is visible in the Fig. 4.10  
 795 (top left), where the radii in the PRF for the lighter particles are bigger than for  
 796 the heavier ones in case of the same  $m_T$  range.

797 In the Fig. 4.9 there is visible scaling in the outward, sideward and longitudi-  
 798 nal direction. Hence one can expect an appearance of such scaling in a direction-  
 799 averaged radius calculated in the LCMS. This radius is presented in the Fig. 4.10  
 800 (bottom) and indeed the  $R_{LCMS}$  exhibits power-law scaling with the  $m_T$ .

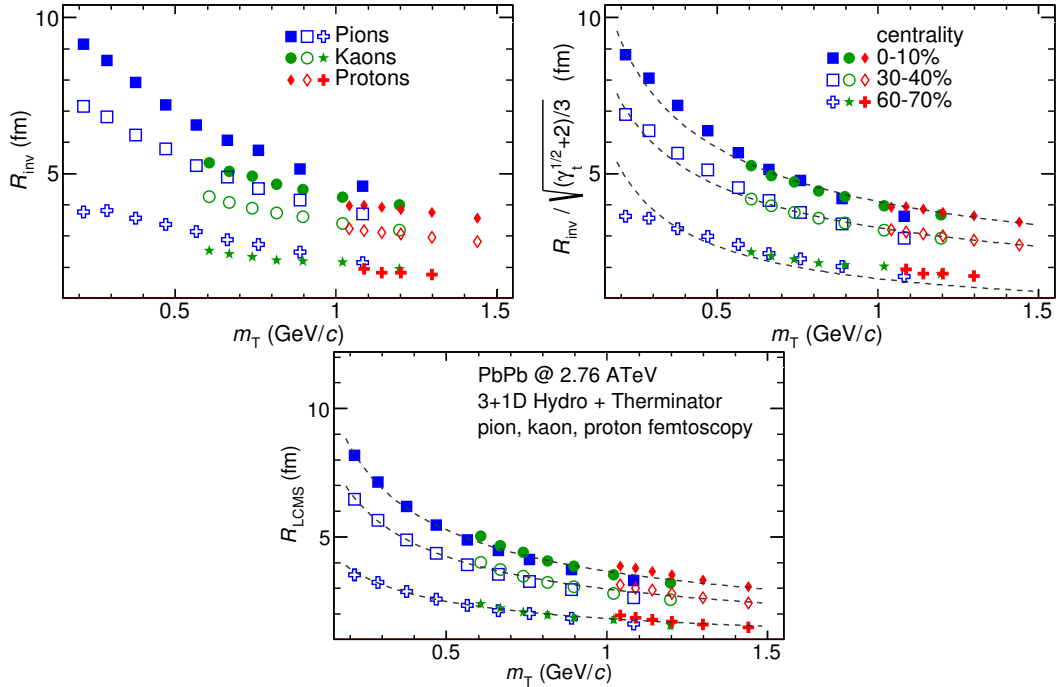


Figure 4.10: Top left: one-dimensional radius for pions, kaons and protons calculated in the PRF. Top right: the  $R_{inv}$  scaled by the proposed factor. Bottom: averaged one-dimensional radius in the LCMS for pions, kaons and protons. Only three centrality bins are shown for the better readability [30].

801 One can try to account the effect of an increase of the radii in the outward  
 802 direction by using the appropriate scaling factor. In the Fig. 4.10 (top right) there  
 803 are femtoscopic radii in the LCMS divided by the proposed scaling factor:

$$f = \sqrt{(\sqrt{\gamma_T} + 2)/3} . \quad (4.3)$$

804 The radii for pions, kaons and protons in the PRF after the division by  $f$  are  
 805 following the power-law with the accuracy of 10%.

### 806 4.3 Discussion of the results

807 The femtoscopic radii obtained from the three-dimensional correlation func-  
 808 tion fitting exhibit the  $m_T$  dependence described by the power law (Eq. 4.1). This  
 809 scaling is preserved quite well with accuracy <10%. Observation of such scaling  
 810 in a femtoscopic radii is a strong signal of appearance of a collective behaviour of  
 811 a particle-emitting source created in the collision. The data used in the analysis  
 812 was coming from the hydrodynamic model, hence one can indeed expect the  
 813 appearance of this scaling. However, the results for pion femtoscopy from the  
 814 ALICE at LHC are consistent with the data from analysis performed in this thesis  
 815 (Fig. 4.6). This is a confirmation of an applicability of hydrodynamic models in a  
 816 description of an evolution of a quark-gluon plasma.

817 The  $\beta$  parameter calculated in the fitting of the power-law to the femtoscopic  
 818 radii is in the order of 0.5 in case of the radii in the transverse plane. This value is  
 819 consistent with the hydrodynamic predictions. In case of longitudinal radii, the  
 820 exponent is bigger (greater than 0.7), which is an indication of a strong transversal  
 821 expansion in the system [28].

822 A scaling described above is visible in the LCMS, however due to limited stat-  
 823 istics, analysis in this reference frame is not always possible. In such case one per-  
 824 forms calculations in the PRF. The  $m_T$  scaling in the PRF is not observed - this has  
 825 the trivial kinematic origin. A transition from the PRF to LCMS causes growth  
 826 of the radius in the outward direction and the common power-law scaling for  
 827 different particles breaks due to differences in the  $\gamma_T(m_T)$  for different particle  
 828 types. However one can try to deal with the radius growth and restore the scal-  
 829 ing by multiplying the radii  $R_{inv}$  by an approximate factor  $\sqrt{(\sqrt{\gamma_T} + 2)/3}$ . The  
 830 scaled  $R_{inv}$  are following the power-law and could be used as a verification of  
 831 hydrodynamic behaviour in the investigated particle source.

832 The hadronic evolution and freeze-out in the THERMINATOR is followed  
 833 by the resonance propagation and decay phase. A good accuracy of a scaling  
 834 with the power-law indicated that the inclusion of the resonances does not  
 835 break the  $m_T$  scaling. However, recent calculations including also hadron  
 836 rescattering phase indicate that the scaling between pions and kaons is broken  
 837 at the LHC [31].

# 838 Conclusions

839 This thesis presents the results of the two-particle femtoscopy of different  
840 particle kinds produced in Pb-Pb collisions at the centre of mass energy  
841  $\sqrt{s_{NN}} = 2.76$  TeV. The analysed data was generated by the THERMINATOR  
842 model using the (3+1)-dimensional hydrodynamic model.

843 The momentum correlations were studied for three different types of particle  
844 pairs: pions, kaons and protons. The data was analyzed for eight different sets  
845 of initial conditions corresponding the following centrality ranges: 0-5%, 0-10%,  
846 10-20%, 20-30%, 30-40%, 40-50%, 50-60% and 60-70%. The correlation functions  
847 were calculated for the nine  $k_T$  bins from 0.1 GeV/c to 1.2 GeV/c. The cal-  
848 culations were performed using spherical harmonics decomposition of a three-  
849 dimensional correlation function. Using this approach, one can obtain full three-  
850 dimensional information about the source size using only the three coefficients:  
851  $\Re C_0^0$ ,  $\Re C_2^0$  and  $\Re C_2^2$ . To perform further quantitative analysis, the femtoscopic  
852 radii were extracted through fitting.

853 The calculated correlation functions show expected increase of a correlation  
854 at low relative momenta in case of identical bosons (pions and kaons) and the  
855 decrease for the identical fermions (protons) respectively. This effect is especially  
856 visible in the first spherical harmonic coefficient  $\Re C_0^0$ . The other two components  
857  $\Re C_2^0$  and  $\Re C_2^2$  are non-vanishing and are providing information about the ratios  
858 of radii in the outward, sideward and longitudinal directions.

859 An increase of width of a correlation function with the peripherality of a colli-  
860 sion and the  $k_T$  is observed for pions, kaons and protons. This increase of femto-  
861 scopic radii (proportional to the inverse of width) with the  $k_T$  is related with the  
862  $m_T$  scaling predicted by the hydrodynamic calculations.

863 Hydrodynamic equations are predicting appearance of femtoscopic radii  
864 common scaling for different kinds of particles with the  $m_T^{-0.5}$  in the LCMS.  
865 In the results in this work, a common scaling for different particle types is  
866 observed in the LCMS in the outward, sideward and longitudinal direction. The  
867 direction-averaged radius  $R_{LCMS}$  also shows this power-law behaviour. The  
868 fitting of a power law  $\alpha m_T^{-\beta}$  to the femtoscopic radii yielded the information,  
869 that the  $\beta$  exponent for the outward and sideward direction is in order of 0.5,  
870 which is consistent with the hydrodynamic predictions. For the longitudinal  
871 direction, the  $\beta$  is bigger ( $>0.7$ ) than in the other directions which is an indication  
872 of a strong transverse flow. Femtoscopic radii in LCMS are following the

873 power-law scaling with the accuracy <5% for pions and kaons, and <10% in case  
874 of protons.

875 In case of the one-dimensional radii  $R_{inv}$  calculated in the PRF, no common  
876 scaling is observed. This is a consequence of a transition from the LCMS to the  
877 PRF, which causes the growth of radius in the outward direction and breaks the  
878 scaling for different particles. However, one can try to correct the influence of  
879 the  $R_{out}$  growth with an approximate factor  $\sqrt{(\sqrt{\gamma_T} + 2)/3}$ . After the division  
880 of the  $R_{inv}$  by the proposed factor, the scaling is restored with an accuracy <10%.  
881 In this way, the experimentally simpler measure of the one-dimensional radii can  
882 be used as a probe for the hydrodynamic collectivity.

883 The THERMINATOR model includes hydrodynamic expansion, statistical had-  
884 ronization, resonance propagation and decay afterwards. The  $m_T$  scaling is pre-  
885 dicted from the pure hydrodynamic calculations. However, this study shows,  
886 that influence of the resonances on this scaling is less than 10%.

887 **Bibliography**

- 888 [1] Standard Model of Elementary Paticles - Wikipedia, the free encyclopedia  
889 [http://en.wikipedia.org/wiki/standard\\_model](http://en.wikipedia.org/wiki/standard_model).
- 890 [2] R. Aaij et al. (LHCb Collaboration). Observation of the resonant character of  
891 the  $z(4430)^-$  state. *Phys. Rev. Lett.*, 112:222002, Jun 2014.
- 892 [3] Donald H. Perkins. *Introduction to High Energy Physics*. Cambridge University Press,  
893 fourth edition, 2000. Cambridge Books Online.
- 894 [4] G. Odyniec. *Phase Diagram of Quantum Chromo-Dynamics* - course at Faculty  
895 of Physics, Warsaw University of Technology, Jun 2012.
- 896 [5] J. Beringer et al. (Particle Data Group). The Review of Particle Physics. *Phys.*  
897 *Rev.*, D86:010001, 2012.
- 898 [6] Z. Fodor and S.D. Katz. The Phase diagram of quantum chromodynamics.  
899 2009.
- 900 [7] F. Karsch. Lattice results on QCD thermodynamics. *Nuclear Physics A*, 698(1-  
901 4):199 – 208, 2002.
- 902 [8] Adam Kisiel. *Studies of non-identical meson-meson correlations at low relative ve-*  
903 *locities in relativistic heavy-ion collisions registered in the STAR experiment*. PhD  
904 thesis, Warsaw University of Technology, Aug 2004.
- 905 [9] J. Bartke. *Relativistic Heavy Ion Physics*. World Scientific Pub., 2009.
- 906 [10] W. Florkowski. *Phenomenology of Ultra-Relativistic Heavy-Ion Collisions*.  
907 World Scientific, 2010.
- 908 [11] Science Grid This Week, October 25, 2006 - Prob-  
909 ing the Perfect Liquid with the STAR Grid  
910 [http://www.interactions.org/sgtw/2006/1025/star\\_grid\\_more.html](http://www.interactions.org/sgtw/2006/1025/star_grid_more.html).
- 911 [12] K. Grebieszkow. Fizyka zderzeń ciężkich jonów,  
912 <http://www.if.pw.edu.pl/~kperl/hip/hip.html>.
- 913 [13] Ulrich W. Heinz. From SPS to RHIC: Maurice and the CERN heavy-ion  
914 programme. *Phys.Scripta*, 78:028005, 2008.

- 915 [14] J. Adams et al. Identified particle distributions in pp and Au+Au collisions  
916 at  $s(\text{NN})^{**}(1/2) = 200 \text{ GeV}$ . *Phys.Rev.Lett.*, 92:112301, 2004.
- 917 [15] G. David, R. Rapp, and Z. Xu. Electromagnetic Probes at RHIC-II. *Phys.Rept.*,  
918 462:176–217, 2008.
- 919 [16] A. Marin et al. Dilepton measurements with CERES. *PoS*, CPOD07:034,  
920 2007.
- 921 [17] J. Adams et al. Experimental and theoretical challenges in the search for the  
922 quark gluon plasma: The STAR Collaboration’s critical assessment of the  
923 evidence from RHIC collisions. *Nucl.Phys.*, A757:102–183, 2005.
- 924 [18] Adam Kisiel, Tomasz Taluc, Wojciech Broniowski, and Wojciech  
925 Florkowski. THERMINATOR: THERMal heavy-IoN generATOR. *Comput.Phys.Commun.*, 174:669–687, 2006.
- 927 [19] Mikolaj Chojnacki, Adam Kisiel, Wojciech Florkowski, and Wojciech Bro-  
928 niowski. THERMINATOR 2: THERMal heavy IoN generATOR 2. *Comput.Phys.Commun.*, 183:746–773, 2012.
- 930 [20] I. et al (BRAHMS Collaboration) Bearden. Charged meson rapidity distri-  
931 butions in central Au + Au collisions at  $\sqrt{s_{\text{NN}}} = 200 \text{ GeV}$ . *Phys. Rev. Lett.*,  
932 94:162301, Apr 2005.
- 933 [21] W. Israel and J.M. Stewart. Transient relativistic thermodynamics and kin-  
934 etic theory. *Annals of Physics*, 118(2):341 – 372, 1979.
- 935 [22] Piotr Bożek. Flow and interferometry in (3 + 1)-dimensional viscous hydro-  
936 dynamics. *Phys. Rev. C*, 85:034901, Mar 2012.
- 937 [23] K. Kovtun, P. D. T. Son, and A. O. Starinets. Viscosity in strongly interacting  
938 quantum field theories from black hole physics. *Phys. Rev. Lett.*, 94:111601,  
939 Mar 2005.
- 940 [24] Fred Cooper and Graham Frye. Single-particle distribution in the hydro-  
941 dynamic and statistical thermodynamic models of multiparticle production.  
942 *Phys. Rev. D*, 10:186–189, Jul 1974.
- 943 [25] Adam Kisiel. Nonidentical-particle femtoscopy at  $\sqrt{s_{\text{NN}}} = 200 \text{ GeV}$  in hy-  
944 drodynamics with statistical hadronization. *Phys. Rev. C*, 81:064906, Jun  
945 2010.
- 946 [26] Adam Kisiel and David A. Brown. Efficient and robust calculation of femto-  
947 scopic correlation functions in spherical harmonics directly from the raw  
948 pairs measured in heavy-ion collisions. *Phys.Rev.*, C80:064911, 2009.
- 949 [27] S. Pratt. Pion Interferometry for Exploding Sources. *Phys.Rev.Lett.*, 53:1219–  
950 1221, 1984.

- 951 [28] S.V. Akkelin and Yu.M. Sinyukov. The HBT-interferometry of expanding  
952 inhomogeneous sources. *Z.Phys.*, C72:501–507, 1996.
- 953 [29] K. Aamodt et al. Two-pion Bose-Einstein correlations in central Pb-Pb colli-  
954 sions at  $\sqrt{s_{NN}} = 2.76$  TeV. *Phys.Lett.*, B696:328–337, 2011.
- 955 [30] A. Kisiel, M. Galazyn, and P. Bozek. Pion, kaon, and proton femtoscopy in  
956 Pb-Pb collisions at  $\sqrt{s_{NN}}=2.76$  TeV modeled in 3+1D hydrodynamics. 2014.
- 957 [31] V.M. Shapoval, P. Braun-Munzinger, Iu.A. Karpenko, and Yu.M. Sinyukov.  
958 Femtoscopy correlations of kaons in  $Pb + Pb$  collisions at LHC within hy-  
959 drokinetic model. 2014.

# 960 List of Figures

961    1.1	The Standard Model of elementary particles [1]. . . . .	2
962    1.2	A string break and a creation of a pair quark-anti-quark [4]. . . . .	4
963    1.3	The coupling parameter $\alpha_s$ dependence on four-momentum trans-	
964    fer $Q^2$ [5]. . . . .		5
965    1.4	The QCD potential for a pair quark-antiquark as a function of dis-	
966    tance for different temperatures. A value of a potential decreases		
967    with the temperature [4]. . . . .		5
968    1.5	A number of degrees of freedom as a function of a temperature [7]. . . . .	6
969    1.6	Phase diagram coming from the Lattice QCD calculations [8]. . . . .	7
970    1.7	Left: stages of a heavy ion collision simulated in the UrQMD	
971    model. Right: schematic view of a heavy ion collision evolution [8].		8
972    1.8	Overlapping region which is created in heavy ion collisions has an	
973    almond shape. Visible x-z plane is a <i>reaction plane</i> . The x-y plane is		
974    a <i>transverse plane</i> . The z is a direction of the beam [11]. . . . .		10
975    1.9	Cross-section of a heavy ion collision in a transverse plane. $\Psi_R$	
976    is an angle between transverse plane and the reaction plane. The		
977 $b$ parameter is an <i>impact parameter</i> - a distance between centers of		
978    nuclei during a collision. An impact parameter is related with the		
979    centrality of a collision and a volume of the quark-gluon plasma [12].		11
980    1.10	<i>Lower:</i> The elliptic flow $v_2$ follows the hydrodynamical predictions	
981    for an ideal fluid perfectly. Note that > 99% of all final hadrons		
982    have $p_T < 1.5 \text{ GeV}/c$ . <i>Upper left:</i> The $v_2$ plotted versus transverse		
983    kinetic energy $KE_T = m_T - m_0 = \sqrt{p_T^2 + m_0^2} - m_0$ . The $v_2$ follows		
984    different universal curves for mesons and baryons. <i>Upper right:</i>		
985    When scaled by the number of valence quarks, the $v_2$ follows the		
986    same universal curve for all hadrons and for all values of scaled		
987    transverse kinetic energy [13]. . . . .		12
988    1.11	Invariant yield of particles versus transverse mass	
989 $m_T = \sqrt{p_T^2 + m_0^2}$ for $\pi^\pm$ , $K^\pm$ , $p$ and $\bar{p}$ at mid-rapidity for p+p		
990    collisions (bottom) and Au+Au events from 70-80% (second		
991    bottom) to 0-5% (top) centrality [14]. . . . .		13

992	1.12	Thermal photons spectra for the central Au+Au collisions at $\sqrt{s_{NN}} = 200$ GeV at computed within different hydrodynamical models compared with the pQCD calculations (solid line) and experimental data from PHENIX (black dots) [15]. . . . .	14
993	1.13	Left: Invariant mass spectrum of $e^+e^-$ pairs in Pb+Au collisions at $158A$ GeV compared to the sum coming from the hadron decays predictions. Right: The expectations coming from model calculations assuming a dropping of the $\rho$ mass (blue) or a spread of the $\rho$ width in the medium (red) [16]. . . . .	15
994	1.14	Azimuthal angle difference $\Delta\phi$ distributions for different colliding systems at $\sqrt{s_{NN}} = 200$ GeV. Transverse momentum cut: $p_T > 2$ GeV. For the Au+Au collisions the away-side jet is missing [17]. . . . .	16
995			
1004	3.1	Bertsch-Pratt direction naming convention used in heavy ion col- lision. . . . .	22
1005	3.2	The pair wave function is a superposition of all possible states. In case of particle interferometry it includes two cases: particles with momenta $p_1, p_2$ registered by detectors $A, B$ and $p_1, p_2$ registered by $B, A$ respectively. . . . .	23
1006	3.3	An averaged three-dimensional Gaussian source function with dif- ferent widths was averaged into one-dimensional function. To il- lustrate deformations, one-dimensional Gaussian distribution was fitted. . . . .	26
1007	3.4	Correlation function width dependence on total pair momentum. Pion pairs with a large total momentum are more correlated [27]. . . . .	30
1008			
1016	4.1	Spherical harmonics coefficients of the two-pion correlation func- tion. From the top left: $\Re C_0^0$ , $\Re C_2^0$ and $\Re C_2^2$ . Only few centrality bins are presented for increased readability. . . . .	33
1017	4.2	Spherical harmonics coefficients of the two-kaon correlation func- tion. From the top left: $\Re C_0^0$ , $\Re C_2^0$ and $\Re C_2^2$ . Only few centrality bins are presented for increased readability. The $\Re C_2^2$ is noisy, but one can still notice that it differs from zero and is becoming negative. . . . .	34
1018	4.3	Spherical harmonics coefficients of the two-proton correlation function. From the top left: $\Re C_0^0$ , $\Re C_2^0$ and $\Re C_2^2$ . Only few centrality bins are presented for increased readability. The $\Re C_2^0$ and $\Re C_2^2$ are noisy, but one can still notice, that they differ from zero and are becoming positive. . . . .	35
1019	4.4	One-dimensional correlation function for pions (top left), kaons (top right) and protons (bottom) for different centralities. . . . .	36
1020			
1021			
1022			
1023			
1024			
1025			
1026			
1027			
1028			
1029			

1030	4.5	One-dimensional correlation functions for pions, kaons and protons, for the same centrality bin and different $k_T$ ranges. The plot was zoomed in to the region which illustrates the $k_T$ dependence in the best way. Only few of the calculated ranges are presented for better readability. . . . .	37
1031			
1032			
1033			
1034			
1035	4.6	Femtoscopic radii in LCMS coming from two-pion correlation functions for all centrality bins as a function of $m_T$ . The dashed lines are power-law fits. The most central collisions (0-5%) are compared to the results from ALICE [29]. The two datasets are shifted to the right for visibility [30]. . . . .	38
1036			
1037			
1038			
1039	4.7	Femtoscopic radii extracted from two-kaon correlation functions for different centrality bins as a function of $m_T$ . [30]. . . . .	39
1040			
1041			
1042	4.8	Femtoscopic radii extracted from two-proton correlation functions for different centrality bins as a function of $m_T$ . [30]. . . . .	40
1043			
1044	4.9	The results from the calculations for the pions, kaons and protons in for the three centralities presented on the common plot. One can notice that radii for particular centralities and different particle types follow the common power-law scaling. [30]. . . . .	41
1045			
1046			
1047			
1048	4.10	Top left: one-dimensional radius for pions, kaons and protons calculated in the PRF. Top right: the $R_{inv}$ scaled by the proposed factor. Bottom: averaged one-dimensional radius in the LCMS for pions, kaons and protons. Only three centrality bins are shown for the better readability [30]. . . . .	42
1049			
1050			
1051			
1052			